Experimentally informed modeling of the early-age stress evolution in cementitious materials using exponential conversion from creep to relaxation

Liang, Minfei; Luzio, Giovanni Di; Schlangen, Erik; Šavija, Branko

DOI
10.1111/mice.13156

Publication date
2024

Document Version
Final published version

Published in
Computer-Aided Civil and Infrastructure Engineering

Citation (APA)
Liang, M., Luzio, G. D., Schlangen, E., & Šavija, B. (2024). Experimentally informed modeling of the early-age stress evolution in cementitious materials using exponential conversion from creep to relaxation. *Computer-Aided Civil and Infrastructure Engineering*, *39*(23), 3507-3530. https://doi.org/10.1111/mice.13156

DOI: 10.1111/mice.13156

RESEARCH ARTICLE

COMPUTER-AIDED CIVIL AND INFRASTRUCTURE ENGINEERING WILEY

Experimentally informed modeling of the early-age stress evolution in cementitious materials using exponential conversion from creep to relaxation

Minfei Liang[1] | **Giovanni Di Luzio**[2] | **Erik Schlangen**[1] | **Branko Šavija**[1]

[1]Microlab, Faculty of Civil Engineering and Geosciences, Delft University of Technology, Delft, The Netherlands

[2]Department of Civil and Environmental Engineering, Politecnico di Milano, Milano, Italy

Correspondence
Erik Schlangen, Microlab, Faculty of Civil Engineering and Geosciences, Delft University of Technology, Delft 2628CN, The Netherlands.
Email: Erik.Schlangen@tudelft.nl

Funding information
China Scholarship Council, Grant/Award Number: 202007000027; European Research Council, Grant/Award Number: 101041342

Abstract

This study presents comprehensive numerical modeling methods for simulating early-age stress (EAS) relaxation in cementitious materials, based on the autogenous deformation (AD), elastic modulus, creep, and stress continuously tested by a mini temperature stress testing machine (Mini-TSTM) and a mini AD testing machine from a very early age (i.e., from a few hours to a week). Four methods for converting creep compliance to relaxation modulus were discussed in detail and used for the one-dimensional (1D) and three-dimensional (3D) simulation of stress evolution in the Mini-TSTM test. Furthermore, virtual creep and relaxation tests were conducted using an exponential algorithm with either the Kelvin or Maxwell chains to show their applicability in simulating the viscoelastic behavior of early-age cementitious materials. The results showed that the exponential algorithm with the Maxwell chain using an exponential conversion function from creep to relaxation obtains good prediction accuracy of EAS in 3D analysis. The numerical solutions of the Volterra integral of creep compliance can lead to a negative relaxation modulus, thus introducing stress calculation errors in both 1D and 3D analysis.

1 | INTRODUCTION

Early-age cracking (EAC) is a common issue in constructing concrete structures. The volumetric deformation, mainly thermal, drying, and autogenous deformation (AD), is the root cause of EAC (Maruyama & Lura, 2019). During the hardening of the cementitious materials, once such volumetric deformation is restrained, often by the structural geometry or other adjacent structural elements, early-age stress (EAS) happens and potentially causes EAC. To quantify the EAC risk, the EAS evolution is a straightforward indication and necessary input for various EAC criteria (Xin et al., 2020). Therefore, developing reliable experimental or numerical tools for testing and predicting EAS evolution is essential for EAC prevention.

There are many experimental methods aiming to quantify the EAS evolution in restrained cementitious materials with different mixture designs and under different environmental conditions, including the internal restraint test (Lura et al., 2009; Semianiuk et al., 2017), rigid cracking frame test (Spingenschmid, 1998), ring test (Briffaut et al., 2016; Shen et al., 2020), and temperature stress testing machine (TSTM; Bjøntegaard, 1999; Igarashi et al., 2000; Klausen, 2016; Klausen et al., 2019; Lokhorst, 2001; Nguyen et al., 2019; Ou et al., 2023; Springenschmid et al., 1994). These tests apply various restraining and

environmental scenarios to mimic the EAC induced by early-age volumetric deformation. Among these tests, TSTM is one of the most comprehensive and advanced testing techniques to simulate various mechanical and thermal boundary conditions with strict control systems of temperature, load, and displacement (Klausen, 2016). Specifically, TSTM enables tests of the EAS and viscoelastic properties with displacement-controlled and load-controlled modes, respectively. Meanwhile, the semi-adiabatic condition that often happens in massive concrete structures can also be simulated with a pre-defined temperature curve input to the TSTM (Xin et al., 2022). In the last two decades, TSTM has been used for investigating multiple influencing factors regarding EAC, including the stress-strength ratio for EAC risk analysis (Igarashi et al., 2000; Xin et al., 2021; Zhu et al., 2020), temperature (Lura et al., 2001), supplementary cementitious materials like granulated ground blast furnace slag (GGBFS; Darquennes et al., 2011; Liang et al., 2023; Shen et al., 2020), fly ash (Xin et al., 2022;), silica fume (Ji et al., 2018), and recycled aggregates (Bendimerad et al., 2020). It was concluded by Klausen et al. (2022) that temperature and restraint degree are the two most influential factors for EAS results, even though considerable variation existed between different batches of the same cement. Similar variations were also systematically investigated by Wyrzykowski et al. (2017).

By analyzing or modeling the EAS evolution based on experimental data, many different studies found that relaxation significantly influences the EAS evolution (Bentur et al., 2001; Li et al., 2021). Creep and relaxation are intrinsic properties of cementitious materials, which mainly originated from the calcium-silicate-hydrate and can be obtained by modeling the creep behavior of cement microstructure using the lattice model (Gan et al., 2021). One major concern about the creep nature of cementitious materials is the long-term deflection, which was well addressed by sophisticated numerical models for creep and shrinkage (Beltempo et al., 2018). To model the EAS evolution, the early-age viscoelastic properties also need necessary inputs to be addressed under different conditions (Azenha et al., 2021; Di Luzio & Cusatis, 2013). Considering the measurements of creep and relaxation, creep tests are much more straightforward than relaxation tests to conduct because creep tests only require recording the deformation under a load-controlled condition. In comparison, the relaxation tests require stress recording under a strain-controlled condition. The strain-controlled condition is achieved by continuous control of the load based on the feedback of deformation measurement, which makes relaxation tests significantly more complex than creep tests. Thereby, to simulate the stress relaxation in the EAS modeling, many studies need to convert the measured creep compliance to relaxation modulus (Bažant & Wu, 1974).

Wei et al. (2017) converted the creep compliance given by the microprestress-solidification (MPS) theory. They successfully predicted the EAS under varying temperatures in restrained concrete with good precision. On the other hand, Li et al. (2021, 2022) also converted the creep compliance to relaxation modulus. In multiple testing cases, they successfully predicted the EAS induced by restrained AD of alkali-activated material. Note that the conversion methods adopted by Wei et al. (2017) and Li et al. (2021, 2022) are entirely different. Wei et al. (2017) used the numerical solution of a linear viscoelastic constitutive equation as a Volterra integral. At the same time, the conversion method adopted by Li et al. (2021, 2022) seems significantly more straightforward, based on a specific solution derived from the definition of relaxation. In addition, it is also worth noting that some methods do not require obtaining the relaxation modulus. Instead, it is also possible to simulate the EAS from the perspective of creep. For example, Klausen (Klausen, 2016) first calculated the incremental creep strain, and then assuming both the AD and creep deformation were restrained, they calculated the incremental EAS with an elastic relation, which also matched well with the experimental observation.

Note that the modeling studies mentioned above were all based on a 1D case since the validation data are from the TSTM test, which is precisely a 1D restraint test. To generalize the obtained creep and shrinkage data to 3D structures and get the corresponding EAS distribution, different numerical methods can be employed, such as finite element method (FEM; Destrebecq & Jurkiewiez, 2001; Xia et al., 2011) or discrete element method (Alnaggar et al., 2017; Cibelli et al., 2022). Simulating the viscoelastic behavior still requires solving Volterra integral (Bažant & Jirásek, 2018). However, solving the Volterra integral is difficult in FEM because, at every time step, the strain/stress history of every previous time step at every Gaussian point needs to be restored, which brings a heavy burden on the computer and the model may be significantly hindered if a large structure with fine meshes is constructed (Di Luzio et al., 2020; Yu et al., 2012). Instead, the exponential algorithm, based either on a Kelvin chain (Bažant & Jirásek, 2018; Di Luzio et al., 2020; Yu et al., 2012) or Maxwell chain (Bažant & Wu, 1974), can be used to solve the Volterra integral with a rate-type form, which then only requires storing a few internal variables of the rheological chains across the modeling process. It should be noted that the Kelvin chain can be calibrated directly by the measured creep data by a continuous retardation chain (Bažant & Xi, 1995; Jirásek & Havlásek, 2014). In contrast, the Maxwell chain needs the relaxation data, so the conversion from creep to relaxation is still required. Due to the better availability of creep data, Kelvin chain has often been used for EAS modeling. Liu & Schindler (Liu & Schindler, 2020) fitted the creep data of the B3 model (Bažant & Baweja, 1994) with

a Kelvin chain and successfully predicted the EAS evolution in a TSTM test by the exponential algorithm. Similarly, Liang et al. (Liang, Chang, et al., 2022; Liang, Li, et al., 2022) implemented the Kelvin chain-based exponential algorithm in simulating the EAS in TSTM tests of GGBFS concrete.

In summary, the studies mentioned above formed a solid basis for testing and modeling the EAS evolution in restrained concrete. However, despite the versatile use of TSTM allowing for testing not only EAS but also creep and elastic modulus, most studies only did the EAS test. They used other (empirical) material models for the input of creep and elastic modulus, compromising their validation reliability. To some extent, the complexity and high cost of TSTM tests hindered a comprehensive experimental campaign to provide first-hand data for validating the modeling results. Moreover, most studies directly implemented the models for EAS prediction, while the difference between these models and their applicability are rarely compared and discussed. This paper presents systematic experiments encompassing the EAS, elastic modulus, and aging creep using a newly designed Mini-TSTM, which aims to improve the testing efficiency significantly, compared to conventional TSTM tests. Based on comprehensive experimental results, four representative numerical models (two for 1D simulation and another two for 3D simulation) will be used to predict the EAS, and their applicability will be discussed. Notably, the prediction results of EAS will be analyzed and compared in detail.

In this paper, the testing and modeling works mainly focus on the cementitious materials within the first week, in which rapid hydration reaction happens and significantly changes the material properties and behaviors. The structure of this paper will be formulated as follows. The second section will introduce the Mini-TSTM and mini AD testing machine (Mini-ADTM), which offer continuous measurement data of AD, elastic modulus, creep, and EAS for the input and verification of the models. Then, the third section will give an overview of the four numerical models for EAS calculations, covering both 1D and 3D simulations. Finally, the experimental and modeling results will be shown in the fourth section. The validity of each numerical model will be analyzed not only from the theoretical aspects but also from the prediction accuracy by comparing the predicted EAS with the tested EAS. In the end, a numerical model is proposed to improve the prediction accuracy of EAS.

2 | MINI TSTM/ADTM TESTS

The experiments of this study are conducted on a Mini-TSTM that was recently developed. The AD, elastic modulus, aging creep, and EAS are tested and used to validate and compare different numerical models.

TABLE 1 Main composition of utilized cements (wt.%).

Composition	CEM III/B	CEM I
CaO	47.11	64.00
SiO_2	29.11	20.00
Al_2O_3	10.02	5.00
MgO	5.89	–
SO_3	2.82	2.93
Fe_2O_3	1.19	3.00
Na_2O	0.28	0.58

2.1 | Materials

The adopted materials in this study are cement paste made of two types of cement, CEM I 42.5N and CEM III/B 42.5N. Both cements were manufactured by the Eerste Nederlandse Cement Industrie. The main chemical compositions of the two cements are listed in Table 1. The adopted w/c ratio is 0.30. Both cement pastes were tested three times, and the experimental results will be termed as C1-30-1, C1-30-2, C1-30-3 and C3-30-1, C3-30-2, C3-30-3.

2.2 | Mini TSTM tests

2.2.1 | The Mini-TSTM setup

The Mini-TSTM system includes molds for two specimens: a dog-bone specimen in restrained condition and a free specimen with similar geometry to the restrained one. A schematic diagram of typical TSTM systems is given in Figure 1. Each specimen contains two bars in its middle section, which are connected to linear variable differential transducers (LVDTs) to measure the deformation of that region (ε_r and ε_s, representing the strain measured by the two bars in the middle of the restrained and unrestrained specimens, respectively). One end of the dog-bone specimen is fixed, while the other is attached to an actuator and a load cell to apply a force F. To regulate the temperature within the specimens, a combination of cryostats, water pipes, and molds with embedded water channels is employed to circulate water. Two feedback control loops, FL1 and FL2, are typically utilized, employing proportional-integral-derivative (PID) controllers. The feedback loop FL1 determines the F force to maintain ε_r at 0, ensuring the full-restraint conditions. To keep the specimen's temperature at a predefined value, the feedback loop FL2 adjusts the temperature of the circulating water T_w, based on the temperature measured by thermocouples within the specimen, T_c.

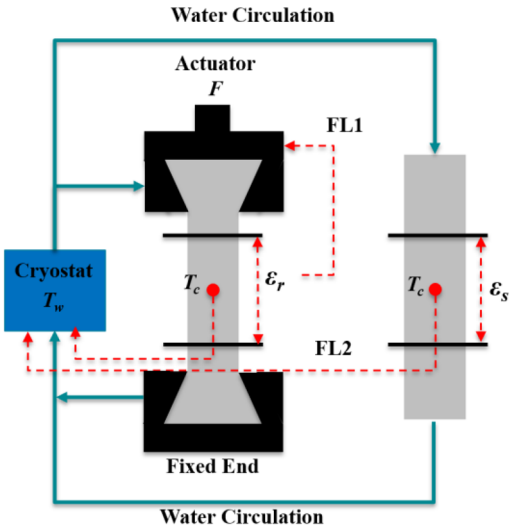

FIGURE 1 Schematic diagram of a temperature stress testing machine (TSTM) system.

The design of the mini-TSTM focuses on simplicity and efficiency as shown in Figure 2. The specimen's total length is 300 mm, with the area of interest being a smaller 50 × 50 × 100 mm^3 middle section (Figure 2c). This compact size allows direct installation into the Instron universal loading machine with a maximum loading capacity of 10 kN. The mini-TSTM can be vertically loaded, minimizing friction, compared to horizontally loaded TSTMs. Note that the 50 × 50 mm^2 section size limits the maximum aggregate size, but it can be increased with a more capable loading machine. The ADTM follows the same design as the TSTM. The Mini-TSTM/ADTM design includes molds, strain measurement, and temperature control.

Molds

As shown in the middle of the Figure 2a, the Mini-TSTM mold is created using stereolithography 3D printing with white powder-based polyamide (PA 2200). The mold consists of covering plates (C1, C2, C3), side plates (S1, S2), crosshead plates (CH1, CH2), and a back plate (B1). The CH1 and CH2 plates are made of steel in the Mini-TSTM, while they are 3D-printed with PA 2200 in the Mini-ADTM. The plates are assembled using bolts, and water channels are incorporated into each plate except for CH1 and CH2. The inner surface of the plates in contact with the specimen is sealed with a copper plate, ensuring effective heat conduction for temperature regulation.

Strain measurements

As shown on the left of Figure 2a, the strain measurement in both the Mini-TSTM and Mini-ADTM involves embedded steel bars, plastic plugs, LVDTs, invar bars, and magnetic blocks. The embedded steel bar, with dimensions of 13.3 mm in length and 3 mm in diameter, is fixed using plugs before casting the fresh mixture. Before the

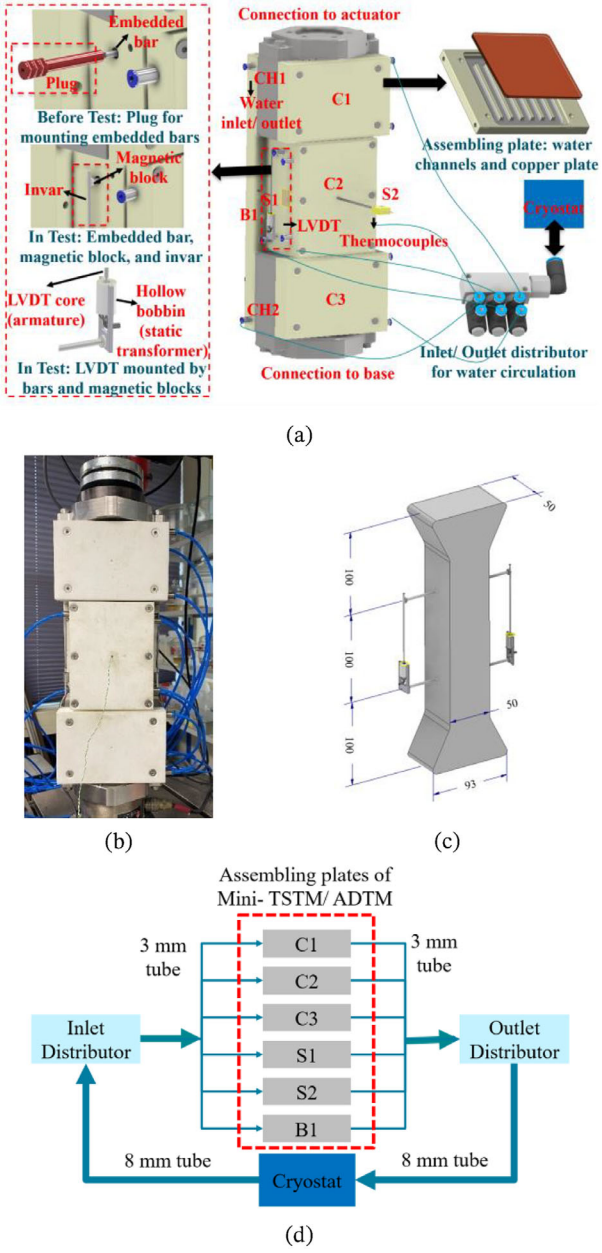

FIGURE 2 The mini-TSTM: (a) overall design, (b) the efficient TSTM installed in the loading machine, (c) geometry of the dog-bone specimen (unit: mm), and (d) parallel connection of water circulation system.

test, the plugs are removed, and LVDTs are attached to the embedded bars. The LVDT is an inductive displacement transducer that requires no contact during measurement. The measurement range of the adopted LVDT is ± 1 mm, and the precision is 0.01 μm. The LVDT consists of a hollow bobbin (static transformer) and a magnetic core (armature). The assembly of the strain measurement components can be seen in Figure 2c: First, the LVDT core should be glued to the lower side of the invar bar; then, with magnetic blocks as the connection, the upper side of the invar bar is attached to the upper embedded bars in the specimen and the LVDT hollow bobbin is attached to

the lower embedded bars. The LVDT core can move in the LVDT hollow bobbin to measure the deformation between the upper and lower embedded steel bars.

Temperature regulation

Figure 2d shows that temperature regulation is achieved by circulating water through plates C1, C2, C3, S1, S2, and B1. These plates have water channels and water inlet/outlet points. A parallel connection is used to circulate the water around the specimen, where heated/cooled water is pumped from the cryostat to the inlet distributor, transported to each plate, and finally sent back to the cryostat via the outlet distributor. The necessary components, such as plastic water tubes, tube joints, water inlet/outlet, and distributors, are manufactured by FESTO. Thermocouples are inserted into the middle of the specimen through the hole of plate C2 to measure the internal temperature. The temperature measured at plate C2, located at the center of the specimen, is used as the controlled objective for the temperature PID controller. Continuous adjustments to the cryostat water temperature ensure that the center temperature of the specimen follows the specified value.

2.2.2 | AD and EAS

The AD was simultaneously measured by the Mini-ADTM and the EAS by the Mini-TSTM. The same batch of material was used for casting the two specimens, and therefore there was no batch difference between the measurement of EAS and AD within each test. The temperature in the specimens was maintained at 20°C by the cryostat, which actively adjusted the water temperature based on the feedback of thermocouples embedded in specimens. A strain-controlled mode was used in the Mini-TSTM test, which ensured a fully restrained condition, and therefore, the EAS induced by AD can be measured. In the Mini-ADTM, the specimens were in free conditions to measure the AD. In this study, the measurement of AD and EAS started 4 h after the placement of fresh material. Note that the choice of 4 h, before the setting time of the utilized material, aims to record the development of AD and EAS as early as possible. Each type of cement was tested three times. In the numerical models, the measured AD will be used as one of the inputs to predict the corresponding EAS.

2.2.3 | Creep and elastic modulus

An hourly repeated load was applied to the specimen to test the elastic modulus and aging creep. Repeated load cycles were used to assess aging creep at different ages, assuming the negligible influence of aging within short time intervals (Delsaute et al., 2016; Irfan-ul-Hassan et al., 2016).

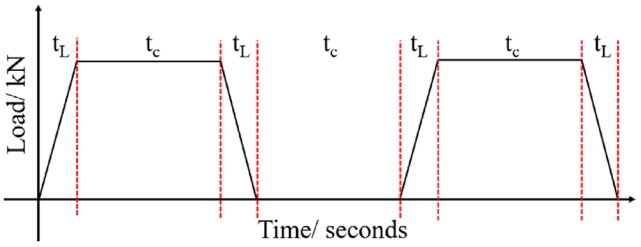

FIGURE 3 Hourly repeated loads for elastic modulus/aging creep test (t_L: 30 s loading time for testing elastic modulus; t_c: 3600 s sustaining at a constant load for testing creep).

The magnitude of the hourly repeated load was determined based on EAS test results, with each cycle lasting 1 h. Figure 3 provides an example of such a repeated load cycle. The hourly repeated loading cycles include a loading phase, a sustained load phase, an unloading phase, and a phase of nearly zero loads. The loading and unloading phases are short ($t_L = 30$ s in this study), allowing measurement of the elastic modulus at a specific age. The loading speed is adjusted to ensure that the duration of the loading/unloading phase is two orders of magnitude smaller than the creep test. The sustained load phase at a specific load typically lasts longer ($t_c = 3600$ s in this study), facilitating the measurement of creep compliance at a certain age. The Mini-TSTM was used to implement such loading cycles, and the Mini-ADTM was used for the AD. Both tests were conducted concurrently with the same batch of cement paste. The creep deformation was obtained by subtracting the AD measured by Mini-ADTM from the total deformation measured by Mini-TSTM. In this study, the hourly repeated loading tests for creep and elastic modulus started 6 h after placement of the fresh material.

After obtaining the aging creep data, a double power function (Bazant & Osman, 1976; Gan et al., 2020) will be fitted to the experimental data as below:

$$J(t_0, t) = \frac{1}{E(t_0)} + a * \left(\frac{1}{t_0}\right)^b * (t - t_0)^c \quad (1)$$

where a, b, and c are fitting parameters that can be derived from tests; t_0 is the time when the load is applied; $(t - t_0)$ is the loading duration. Each type of cement was tested once, and the results of elastic modulus and creep compliance function will be used as input for the models to predict EAS.

3 | MODELS

Modeling the EAS requires three time-dependent inputs: the AD, the elastic modulus, and the relaxation modulus. In this study, the AD was measured by the Mini-ADTM

by specifying a free mechanical boundary and constant temperature. The elastic modulus and creep were measured by the Mini-TSTM using an hourly repeated loading scheme. The Mini-TSTM also measured the EAS with a fully restrained boundary condition and then was used to validate four proposed models. Conversion from creep to relaxation is a crucial step in the simulation of EAS evolution and will be the key focus of this study.

3.1 | Theory

EAS evolution in restrained concrete results from a non-stop relaxation test: During the hardening of cementitious materials, within every time interval, an imposed deformation is applied to the hardening concrete to compensate for the AD and keep the specimen fully restrained, which then induces EAS. If the concrete material is linearly elastic, then the EAS in each time interval should be expressed as

$$\Delta\sigma\left(t_0\right) = E\left(t_0\right)\Delta\varepsilon\left(t_0\right) \tag{2}$$

where t_0 is the time when the imposed deformation $\Delta\varepsilon$ is applied. Then, under the assumption of Boltzmann superposition, the total EAS at time t should be the integration of the elastic modulus E over the imposed deformation, expressed as

$$\sigma\left(t\right) = \int_0^t E\left(t_0\right)\mathrm{d}\varepsilon\left(t_0\right) \tag{3}$$

However, it is clear that the cementitious materials are viscoelastic, and the relaxation of stress should be taken into consideration under any circumstances (Azenha et al., 2021). Therefore, in Equation (3), instead of the elastic modulus, the relaxation modulus $R\left(t_0, t\right)$ should be used, expressed as

$$\sigma\left(t\right) = \int_0^t R\left(t_0, t\right)\mathrm{d}\varepsilon\left(t_0\right) \tag{4}$$

Equation (4) is the exact solution of EAS, a Volterra integral obtained by the Boltzmann superposition. Using the mid-point rule, EAS results can be obtained, expressed as

$$\sigma\left(t\right) = \sum_{t_0=0}^{t_0=t} R\left(t_0 + \frac{1}{2}\Delta t_0, t\right) \times \Delta\varepsilon\left(t_0\right) \tag{5}$$

Equation (5) gives the numerical solution of EAS. It is clear that only two inputs are required: (1) relaxation modulus for viscoelasticity $R\left(t_0, t\right)$ and (2) rate of AD $\Delta\varepsilon$. The $\Delta\varepsilon$ can be directly obtained from the test. However, the $R(t_0,t)$ requires a conversion from creep compliance to relaxation modulus since most tests for viscoelasticity are creep tests. Creep compliance function $J(t_0,t)$ and relaxation modulus function $R(t_0, t)$ are fully coupled if linear viscoelasticity is applied. Given a stress history $\sigma(t)$ applied at t_0 and continuously last until t_f, the strain at t_f can be expressed as

$$\varepsilon\left(t_f\right) = J\left(t_0, t_f\right)\sigma\left(t_0\right) + \int_{t_{0+}}^{t_f} J\left(t', t_f\right)\sigma\left(\dot{t}'\right)\mathrm{d}t' \tag{6}$$

Then, considering a relaxation test and the definition of relaxation modulus, Equation (6) can be easily rewritten as

$$J\left(t_0, t_f\right)R\left(t_0, t_0\right) + \int_{t_{0+}}^{t_f} J\left(t', t_f\right)R\left(\dot{t}_0, t'\right)\mathrm{d}\,t' = 1 \tag{7}$$

Equation (7) gives the exact relationship between creep and relaxation. Substituting the creep compliance $J(t_0, t)$ in Equation (7) allows the derivation of relaxation modulus $R(t_0, t)$, which will form the basis of the first model in this study and will be introduced in Section "Model 1 (M1): Numerical solution of the integral form". Moreover, substituting the obtained creep compliance function $J(t_0, t)$ and relaxation modulus function $R(t_0, t)$ in the left of Equation (7), the results should be close to 1.0 as much as possible. This checking process can be applied to check the conversion process from creep to relaxation and will be termed "integral check" in the following part of the paper. Given the creep compliance function $J(t_0, t)$ and relaxation modulus function $R(t_0, t)$, Equation (7) can be solved as follows:

$$J\left(t_0, t_f\right)R\left(t_0, t_0\right) + \sum_{i=t_0+1}^{t_f} J\left(t_{i+1/2}, t_f\right)\left[R\left(t_0, t_i\right) - R\left(t_0, t_{i-1}\right)\right] = 1 \tag{8}$$

3.2 | EAS modeling

This study investigated two types of EAS models: models for 1D analysis and 3D analysis.

3.2.1 | Models for 1D analysis

The 1D analysis model only considers the case of a shrinking bar that is fully restrained at the two ends. Because the TSTM tests are also uniaxial loading tests, the 1D analysis applies to EAS calculation in TSTM tests. In 1D analysis, Equations (4) and (5) can directly calculate the corresponding EAS. A significant problem with 1D analysis lies in converting from a creep compliance function

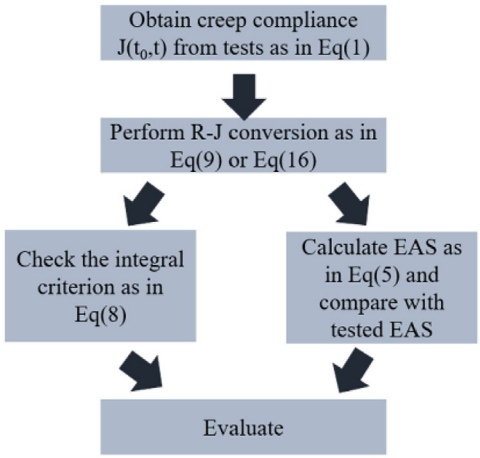

FIGURE 4 Procedures of 1D analysis.

to a relaxation modulus function. For 1D analysis, two representative methods will be used to conduct such conversions. The obtained relaxation modulus function will be analyzed by the integral check using Equations (7) and (8). The final validation will be done by comparing the tested and predicted EAS. The working procedures for the 1D analysis are shown in Figure 4.

Model 1 (M1): Numerical solution of the integral form

The conversion from creep to relaxation in Model 1 (M1) is done by substituting the creep compliance into Equation (7) and solving the corresponding relaxation modulus numerically. Therefore, M1 is intrinsically based on the numerical solution of the integral form. Wei et al. (2017) applied M1 to transfer the creep compliance function adjusted by MPS theory and successfully predicted the EAS under varying temperatures. Given the creep compliance function $J(t_0, t)$, the relaxation function $R(t_0, t)$ can be obtained numerically as below (Bažant & Jirásek, 2018):

$$R(t_0, 1) = 0 \tag{9.1}$$

$$R(t_0, 2) = \frac{1}{J(t_0, t_0)} \tag{9.2}$$

$$R(t_0, k+1) = R(t_0, k) - \frac{1}{J_{k,k+1}} \sum_{i=1}^{k-1} \Delta J_{i,k} \left(R(t_0, i+1) - R(t_0, i)\right) \tag{9.3}$$

$$J_{k,k+1} = \frac{J(k+1, k+1) + J(k, k+1)}{2} \tag{9.4}$$

$$\Delta J_{i,k} = J(k, i+1) - J(k, i) \tag{9.5}$$

It should be noted that the first term as in Equation (9.1) is merely an auxiliary term that enables to start the iteration in Equation (9.4). However, due to the high non-linearity of the relaxation modulus at the beginning, directly implementing the numerical solution, as in Equation (9), can lead to an underestimation of the relaxation modulus. Therefore, instead of following the initial conditions as in Equation (9.2), it was also suggested to keep the second and third term of the relaxation modulus constant (Bažant & Jirásek, 2018), expressed as below:

$$R(t_0, 2) = R(t_0, 3) = \frac{1}{J(t_0, t_2)} \tag{10}$$

It should be noted that the initial conditions as in Equation (10) are merely used for calculating the other relaxation modulus after $t = 3$, while the real relaxation modulus of the first two terms stays the same as in Equations (9.1) and (9.2).

Model 2 (M2): An explicit exponential conversion from creep to relaxation

Model 2 (M2) was initially proposed by Wittmann (1974) and Van Breugel (1980) to calculate the EAS in young concrete and obtain good prediction accuracy with ordinary concrete. Recently, M2 has also been applied to alkali-activated materials and showed good applicability (Li et al., 2021, 2022). Assuming the total strain is composed of two parts, the elastic and the creep part, which can be expressed as below:

$$\varepsilon = \varepsilon_{el} + \varepsilon_c \tag{11}$$

where ε_{el} and ε_c are the elastic and creep strain, respectively. Note that with the definition of relaxation tests, the total strain is a constant independent of time. Then, by taking the derivative at the two sides and expressing the elastic strain with Hooke's law, one gets:

$$\frac{1}{E(t_0)} \frac{d\sigma}{dt} = -\frac{d\varepsilon_c}{dt} \tag{12}$$

Assuming that the creep strain at a certain t_0 can be expressed by power functions (Bažant & Jirásek, 2018; Bazant & Osman, 1976; that is, $J(t_0, t) = a(t - t_0)^n$), the Equation (12) can be rewritten as

$$\frac{1}{E(t_0)} \frac{d\sigma}{dt} = -\sigma a n (t - t_0)^{n-1} \tag{13}$$

Note that a and n are fitting parameters of the power function of creep. Integrating Equation (13) leads to:

$$ln\sigma = -E(t_0)\, a\, (t - t_0)^n + C \tag{14}$$

where C is a constant depending on the initial condition. Assuming the initial stress is σ_0, the ratio of stress σ and σ_0

can be obtained as below:

$$\frac{\sigma}{\sigma_0} = e^{-E(t_0)a(t-t_0)^n} \tag{15}$$

Therefore, the relaxation modulus can be written as

$$R(t_0, t) = e^{1-J(t_0,t)E(t_0)}\, E(t_0) \tag{16}$$

Note that the exponent in Equation (16) is the creep coefficient. It should also be noted that M2 is significantly more straightforward to handle than M1 because Equation (16) can be directly solved. On the contrary, M1 needs a more complex numerical scheme, as in Equations (9) and (10), to obtain the relaxation modulus. By substituting the tested elastic modulus and creep compliance into Equation (16), one gets the relaxation modulus explicitly, and then the EAS can be calculated directly by Equation (5).

3.2.2 | Models for 3D analysis

For the final aim to assess the EAS in real concrete structures, the FEM method should be used for 3D analysis. Because solving the Volterra integral Equations (4) and (5) in FEM will be computationally expensive, this study employed the exponential algorithm (Bažant & Jirásek, 2018; Bažant & Wu, 1974; Di Luzio et al., 2020; Yu et al., 2012) based on the Kelvin chain model and Maxwell chain model, which turns the Volterra integral into a rate-type form and allows to solve it with a quasi-elastic constitutive relationship. The exponential algorithm is also based on the integral formation of Equations (4) and (6). The first step of the exponential algorithm is to reformulate Equations (4) or (6) in the following incremental form:

$$\Delta\sigma = E^*(\Delta\varepsilon - \Delta\varepsilon_{ad}) - \sigma^* \tag{17}$$

where E^* is the incremental modulus; σ^* is an internal variable in the rheological chain that should be updated in each computation cycle; $\Delta\varepsilon_{ad}$ is the incremental AD. The adopted Kelvin chain or Maxwell chain gives the exact solution of the E^* and σ^* that will be introduced in detail in the following sections. First, using Equation (17) as the constitutive equation and setting $\Delta\varepsilon_{ad}$ to 0, virtual uniaxial creep/relaxation tests will be conducted on a 150 × 150 × 750 prism (Figure 5a). The boundary condition of creep/relaxation tests is formulated by fixing the bottom of the prism and applying unit load/displacement on the top. Creep/relaxation tests aim to check the applicability of the exponential algorithm in simulating the viscoelastic behavior in FEM. Then, a virtual Mini-TSTM test will be conducted based on a dog-bone specimen restrained at the two ends and with the same geometry as the Mini-TSTM specimen (Figure 5b). The measured AD in the Mini-ADTM is then used as input of $\Delta\varepsilon_{ad}$.

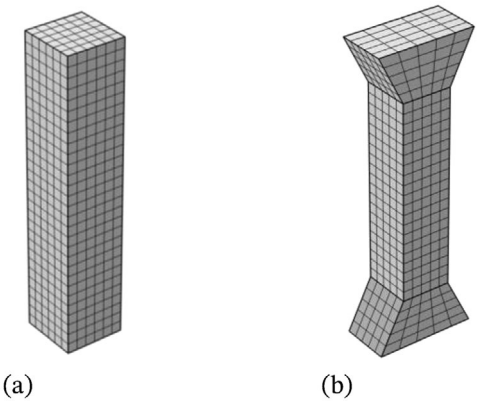

FIGURE 5 Virtual specimens in finite element method (FEM) simulation of viscoelastic behavior: (a) prism for basic creep/relaxation tests and (b) dog-bone specimen for Mini-TSTM tests.

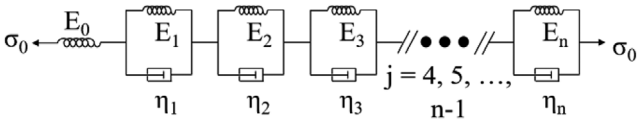

FIGURE 6 A Kelvin chain with *n* units.

Because the integral check requires solving Equations (7) and (8) at every t_0 and t, which is very computationally expensive for FEM, this study only checks the coupling between creep and relaxation in FEM with virtual creep/relaxation tests at four different ages, including 7, 24, 48, and 72 h. The final validation of the FEM will still be using the tested AD, elastic modulus, and creep to calculate the EAS, and then the calculated EAS can be compared to the tested EAS.

Model 3 (M3): Exponential algorithm based on Kelvin chain

A typical Kelvin chain with n units is shown in Figure 6. Solving the system of the differential equations of rheological units, the creep compliance function can be obtained then by adding the strain in each rheological unit under a constant unit load, which then can be expressed as

$$J(t_0, t) = \frac{1}{E_0(t_0)} + \sum_{j=1}^{n} \frac{1}{E_j(t_0)} \left(1 - e^{-\frac{t-t_0}{\mu_j}}\right) \tag{18}$$

where E_j and η_j are the elastic modulus of the spring and viscosity coefficient in the j-th rheological unit, respectively, and μ_j is the retardation time of jth unit and $\mu_j = \eta_j/E_j$.

Rewrite Equation (6) into the incremental form as Equation (17) and substitute the creep compliance function in Equation (18) into the incremental form derived from Equation (6), one obtains the numerical solution of incremental modulus E^* and internal variable σ^* as below (Bažant & Jirásek, 2018; Di Luzio et al., 2020; Yu et al., 2012):

$$E^*(t^*) = \frac{1}{\frac{1}{E_0(t^*)} + \sum_{j=1}^{n} \frac{1}{E_j(t^*)} \left(1 - \left(1 - e^{-\frac{\Delta t}{\mu_j}}\right) \frac{\mu_j}{\Delta t}\right)} \tag{19.1}$$

$$\sigma^*(t_i) = E^*(t^*) \sum_{j=1}^{n} \left(1 - e^{-\frac{\Delta t}{\mu_j}}\right) \varepsilon_j^*(t_i) \tag{19.2}$$

$$\varepsilon_j^*(t_{i+1}) = e^{-\frac{\Delta t}{\mu_j}} \varepsilon_j^*(t_i) + \frac{1}{E^*(t_i)} \left(1 - e^{-\frac{\Delta t}{\mu_j}}\right) \frac{\mu_j}{\Delta t} \Delta\sigma \tag{19.3}$$

where t^* is the average of two consecutive time steps t_i and t_{i+1}. Equations (17) and (19) encompass the incremental viscoelastic constitutive relationship for simulating the development of stress induced by AD. Note that the ε^* of each Kelvin chain unit is the internal state variable, a second-order strain tensor that must be updated on each integration point according to Equation (19.3) at every time step.

It is important to note that the input of the Kelvin chain is creep compliance as in Equation (18). Therefore, implementation of Model 3 (M3) requires determining the parameters of the adopted Kelvin chain (i.e., E_j and μ_j in Equation 18) by fitting Equation (18) with the tested creep compliance function (i.e., Equation 1 fitted by the tested creep data). In this study, a 13-unit Kelvin chain is used. Note that the number of Kelvin chain units can influence the fitting accuracy of the creep compliance function using Equation (18), and insufficient units can lead to underfitting. In our study, the 13-unit Kelvin was carefully selected by parameter studies beforehand and is sufficient to fit the creep compliance function, which will be shown in the result analysis in Section 4.3.1. Using the continuous retardation spectrum method (Bažant & Xi, 1995; Di Luzio et al., 2020), the retardation time μ_j is chosen as a priori to prevent an ill-conditioned equation system as below:

$$\mu_j = 10^{-7+j}, \mathrm{j} = 1 : 13 \tag{20}$$

Then the continuous fitting form for the non-aging term in Equation (1) (i.e., $C(t-t_0) = (t-t_0)^c$) is as follows:

$$C(t-t_0) = \int_0^{\infty} \frac{1}{E_j} \left(1 - e^{-\frac{t-t_0}{\mu_j}}\right) \mathrm{d}\left(\ln \mu_j\right) \tag{21}$$

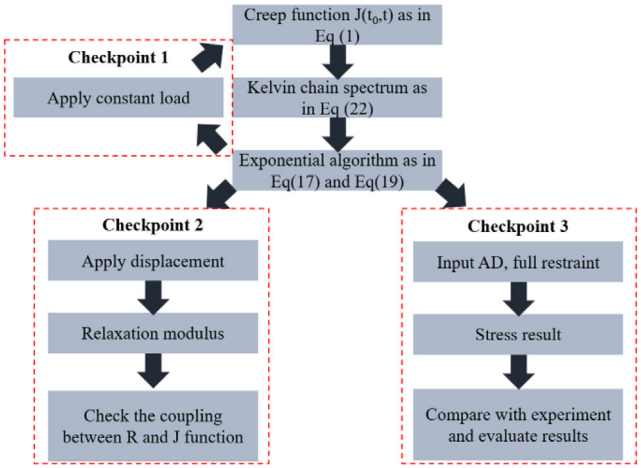

FIGURE 7 Procedures for exponential algorithm based on Kelvin chain.

Using the Laplace transform and Widder's formula, the solutions of E_j can be derived (Bažant & Xi, 1995):

$$\frac{1}{E_j} = -\ln 10 * \lim_{k\to\infty} \frac{(-k\mu)^k}{(k-1)!} C^k(k\mu) \tag{22}$$

In this study, the spectrum of third order ($k = 3$) is used, which was proved to achieve high accuracy in fitting Kelvin chain parameters (Bažant & Xi, 1995; Di Luzio et al., 2020). The working procedures for the M3 are shown in Figure 7. Three checkpoints are proposed to examine the feasibility of the M3: (1) by doing a virtual creep test, the obtained creep compliance function should be the same as the input creep compliance function; (2) by doing a virtual relaxation test, the obtained relaxation modulus should show a similar coupling as obtained by M1; (3) by doing a Mini-TSTM test, which uses the AD tested by the Mini-ADTM as the input, the obtained EAS should match the tested EAS.

Model 4: Exponential algorithm based on Maxwell chain

Model 4 (M4) is based on the Maxwell chain, as shown in Figure 8. By solving the system of differential equation of the Maxwell chain with n units, the relaxation modulus can be explicitly expressed as

$$R(t_0, t) = E_0(t_0) + \sum_{j=1}^{n} E_j(t_0) e^{-\frac{t-t'}{\mu_j}} \tag{23}$$

Similarly, by substituting Equation (23) into the incremental from as in Equation (17) derived by Equation (4), one obtains the numerical solution of modulus E^* and internal variable σ^* as below (Bažant & Wu, 1974):

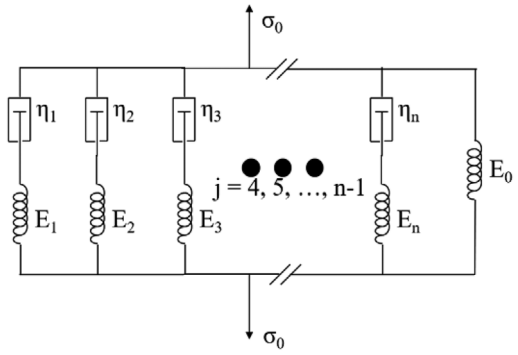

FIGURE 8 A Maxwell chain with n units.

$$E^*(t^*) = \sum_{j=1}^{N} E_j(t^*)\left(1 - e^{-\frac{\Delta t}{\mu_j}}\right)\frac{\mu_j}{\Delta t} + E_0(t^*) \quad (24.1)$$

$$\sigma^*(t_{i+1}) = \sum_{j=1}^{n}\left(1 - e^{-\frac{\Delta t}{\mu_j}}\right)\sigma_j^*(t_i) + E^*(t_{i+1})\Delta\varepsilon_{ad}(t_{i+1}) \quad (24.2)$$

$$\sigma_j^*(t_i) = e^{-\frac{\Delta t}{\mu_j}}\sigma_j^*(t_{i-1}) + E^*(t^*)\left(1 - e^{-\frac{\Delta t}{\mu_j}}\right)\frac{\mu_j}{\Delta t}(\Delta\varepsilon(t_i) - \Delta\varepsilon_{ad}(t_i)) \quad (24.3)$$

Equations (17) and (24) form the exponential algorithm based on the Maxwell chain and can be implemented in FEM to simulate the viscoelastic behaviors. However, it should be noted that the Maxwell chain-based model requires an input of relaxation modulus as shown in Equation (23). Therefore, the tested creep compliance function, as in the form of Equation (1), should be converted to a relaxation modulus function before it can be used as input for the Maxwell model. In this study, we used the conversion method as given by M2 (i.e., Equation 16) to do such a conversion. The reason for using M2 is its simplicity, and the converted relaxation modulus of M2 is more consistent. A detailed explanation for this can be found in Section 4.2. After the relaxation modulus is available, the nonlinear optimization tool (Byrd et al., 1999, 2000; Coleman & Li, 1994, 1996; Gill et al., 1981; Han, 1977; Powell, 1978a, 1978b; Waltz et al., 2006) developed by MATLAB is adopted to complete the fitting process of the Maxwell chain spectrum. Note that the studied time range in this paper is from 0 to 168 h after the placement of fresh material, with 1 h as the time step. Assuming that the adopted Maxwell chain has 13 units and the retardation time is selected as Equation (20), then the objective of the optimization process is to find the E_j ($j = 1, 2, \ldots, 13$) that can make the relaxation modulus derived by the Maxwell chain (i.e., Equation 23) as similar as the relaxation modulus converted from the tested creep compliance. The 13-unit Maxwell chain was chosen to maintain consistency with the Kelvin chain and to better fit the relaxation modulus. Therefore, this study's retardation spectrum of the Maxwell chain would be a 168×13 array, with the first axis corresponding to the loading time and the second axis corresponding to the jth unit in the Maxwell chain.

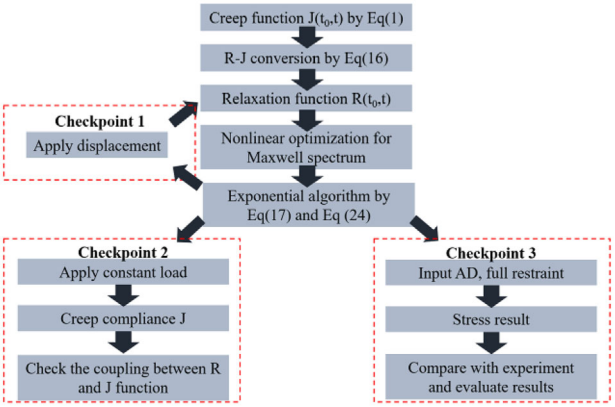

FIGURE 9 Procedures for exponential algorithm based on Maxwell chain.

The working procedure for the exponential algorithm based on the Maxwell chain is formulated in Figure 9. Three checkpoints are proposed to examine the feasibility of the M3: (1) by doing a virtual relaxation test, the obtained relaxation modulus function should be the same as the input relaxation modulus function; (2) by doing a virtual creep test, the obtained creep compliance should show a similar coupling as obtained by M2; (3) by doing a Mini-TSTM test, which uses the AD tested by the Mini-ADTM as the input, the obtained EAS should match the tested EAS.

4 | RESULTS AND DISCUSSIONS

4.1 | Experimental results

4.1.1 | AD and EAS

The experimental results of the AD and EAS of the two types of cement pastes are shown in Figure 10. Note that despite the same type of cement being used, different batches of cement still cause different testing results, especially for the early AD. Such considerable variation was also observed and highlighted by the studies that systematically investigated the variations in TSTM and AD tests (Klausen et al., 2022; Wyrzykowski et al., 2017). However, it should be noted that such batch difference does not exist in a single test because the specimens for EAS measurement in Mini-TSTM and specimens for AD in Mini-ADTM were cast from the same batch of fresh material and tested simultaneously. Detailed analysis of the experimental results is as follows.

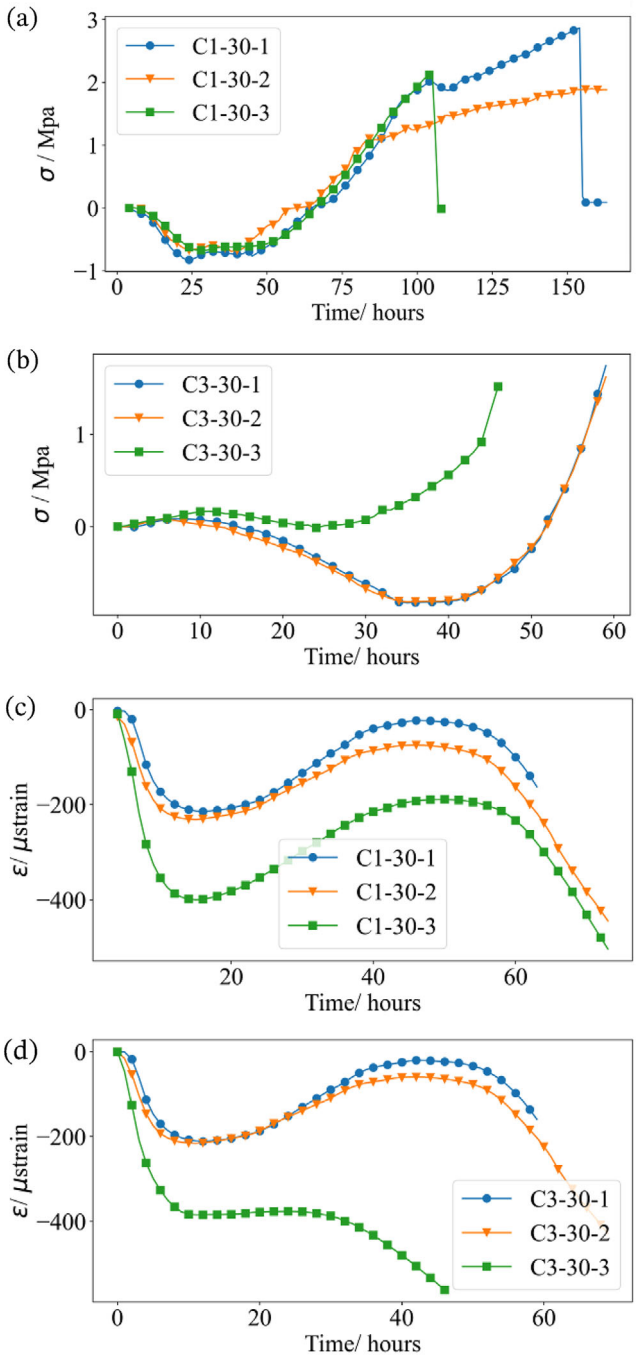

FIGURE 10 Experimental results of Mini-TSTM test in fully restrained and free conditions: (a, c) early-age stress (EAS) and autogenous deformation (AD) of CEM I 42.5N paste; (b, d) EAS and AD of CEM III/B 42.5N paste.

The AD of both C1 and C3 paste can basically be divided into three stages: a fast shrinkage in the first 10 h, followed by an expansion until about the second day, and finally shrinkage starting after approximately 2–3 days.

Within each test, the EAS evolution in Figure 10a,b matches the corresponding AD in Figure 10c,d. Precisely, the increasing/decreasing of stress (i.e., tension/compression) corresponds to the shrinking/expanding process. Note that the EAS induced by initial fast shrinkage in the first 10 h is minor because of the very low elastic modulus and high relaxation. The following numerical results will prove that each of the ADs can be used to correctly predict the corresponding EAS with the viscoelastic properties of the material given as another input, which demonstrates that each measurement of AD under free condition is an exclusive description of the EAS evolution tested under fully restrained condition.

Significant variation exists in measuring the first two stages of C1 paste's AD. However, such variation of AD only induces limited variation in the measurement of EAS because of the low elastic modulus and high relaxation in corresponding ages, which will be proved in the following numerical modeling works.

Despite some variation in the AD, C3-30-1 and C3-30-2 showed almost a perfect match in the EAS measurement. Moreover, it should be noted that the C3-30-3 showed significantly different behavior. C3-30-3 did not expand in the first 2 days like the C3-30-1 and C3-30-2. The autogenous expansion in high-volume slag cement like C3-30-1 and C3-30-2 was observed by many other studies (Carette & Staquet, 2018; Darquennes et al., 2011; Liang et al., 2023), and such expansion was attributed to fast ettringite formation. However, the AD of C3-30-3 is not the result of measurement artifact because in the EAS result of C3-30-3, the EAS from 10 to 20 h also stabilized, corresponding to the platform in Figure 10d. After 30 h, the tensile EAS gradually built up, corresponding to the onset of shrinkage in Figure 10d. The EAS evolution of C3-30-3 perfectly matched AD's corresponding measurement; therefore, the material behavior was correctly measured and recorded by the Mini-TSTM and ADTM setups. The exact reason why C3-30-3 displayed no expansion may lie in the composition variation between different batches of CEM III/B 42.5N and is not the focus of this study, which aims for testing and modeling of stress relaxation and only requires a match between the specimens in Mini-ADTM test and Mini-TSTM test.

In the numerical study, the results of AD in Figure 10c,d were used as the input for the proposed four models M1–M4 (see Equations 5 and 17) to calculate the EAS. The predicted EAS was then compared to the results of EAS in Figure 10a,b.

4.1.2 | Creep and elastic modulus

Besides the AD, another essential input for the models M1–M4 is the viscoelastic properties, which are relevant to $R(t_0, t)$ in Equation (5) and E^*, σ^* in Equation (17).

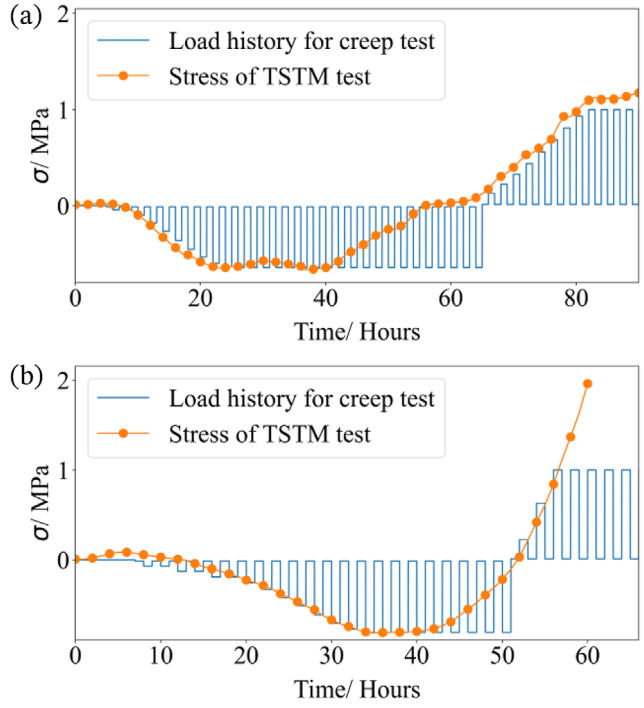

FIGURE 11 Hourly repeated loading cycles for the elastic modulus and aging creep for (a) CEM I 42.5N paste and (b) CEM III/B 42.5N paste.

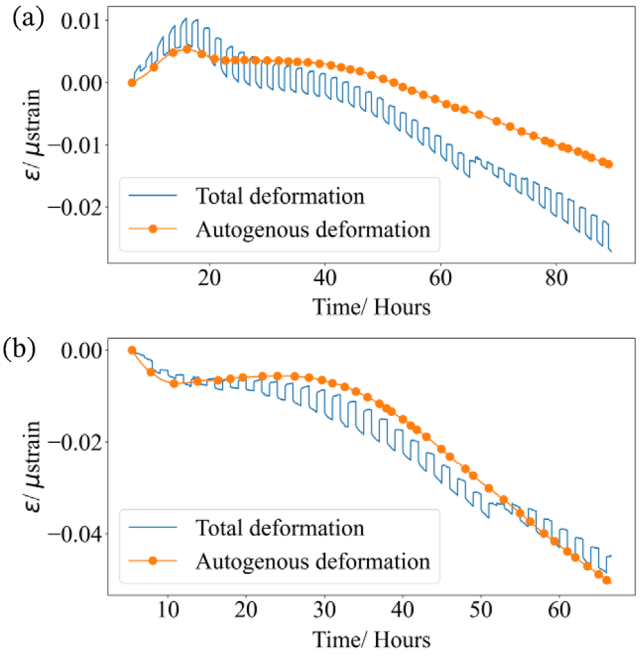

FIGURE 12 Results of the hourly repeated loading tests: (a) CEM I 42.5N paste and (b) CEM III/B 42.5N paste.

The viscoelastic properties in this study are quantified by measuring the elastic modulus and aging creep by hourly repeated loading cycles as introduced in Section 2.2.3. The hourly repeated loading scheme was made according to the EAS results C1-30-1 and C3-30-1 in Figure 10a,b, shown in Figure 11.

Accordingly, the total deformation measured in the Mini-TSTM and the AD measured in the Mini-ADTM can be obtained as shown in Figure 12. It is clear that the total deformation curve is the superimposition of creep deformation and AD. The deformation in each loading/unloading phase, as shown in Figure 12, is used to calculate the elastic modulus at each time point, using the load history as reported in Figure 11. Similarly, the deformation within each load-sustaining phase is used to calculate the creep compliance, employing the load history in Figure 11. Note that the creep strain is obtained by subtracting the AD from the total deformation.

Based on the deformation in each loading/unloading phase and the load-sustaining phase in Figure 12, and combining the load history in Figure 11, the elastic modulus and creep compliance at each time point can be calculated. The results of the time-dependent elastic modulus and creep compliance function are given by Equations (25) and (26). The elastic modulus was fitted according to an empirical function similar to the expression of elastic modulus in the American Concrete Institute (ACI) code (American Concrete Institute & ACI Committee 209–Creep and Shrinkage, 2008), and the creep function was modeled according to Equation (1). Note that this study focuses on early-age creep, and therefore a power-law function (Bazant & Osman, 1976) is used. A logarithmic function (Baronet et al., 2022) should be more appropriate for long-term creep.

For CEM I 42.5N paste, the results are as follows:

$$J(t_0,t) = \frac{1}{E(t_0)} + 0,100*\left(\frac{1}{t_0}\right)^{1,079} * (t-t_0)^{0,5} \quad (25.1)$$

$$E(t_0) = 26,46*\frac{t_0}{0,7337*10^5 + 0,9519*t_0} \quad (25.2)$$

where the elastic modulus E is in GPa; t and t_0 are in seconds; creep compliance J is in μstrain/MPa. For CEM III/B 42.5N paste, the results are as below:

$$J(t_0,t) = \frac{1}{E(t_0)} + 0,362*\left(\frac{1}{t_0}\right)^{1,197} * (t-t_0)^{0,5} \quad (26.1)$$

$$E(t_0) = 31,79*\frac{t_0}{1,535*10^5 + 0,5453*t_0} \quad (26.2)$$

The units of variables are the same as in Equation (25). Equations (25) and (26) are the inputs of viscoelastic properties for the models M1–M4 to simulate stress relaxation in a fully restrained Mini-TSTM test.

4.2 | The 1D analysis for conversion from creep to relaxation

The 1D study was conducted by M1 and M2 as introduced in Section 3.2.1. In this section, the conversion results of M1 and M2 will be analyzed, and the integral check will be performed.

4.2.1 | Conversion results

After obtaining the viscoelastic properties as in Equations (25) and (26), the conversion from creep to relaxation can be done by M1 (i.e., Equations (9) and (10) or M2 (i.e., Equation 16). The conversion results of the two types of cement paste are shown in Figure 13. Note that in this study, the interested time range is 1–168 h, with a time step of 1 h. Therefore, the relaxation modulus $R\ (t_0,\ t)$ is a 168 × 168 array. To clearly display the relaxation modulus $R\ (t_0,\ t)$, only 16 sets of $R\ (t_0,\ t)$ are shown below, with t_0 equal to 10, 20, 30, …, and 160 h. As expected, the relaxation modulus obtained by both M1 and M2 follows a clear decreasing trend. However, the results of M1 (Figure 13a,c) do not converge to 0 but to negative values. In comparison, the results obtained by M2 (Figure 13b,d) always converge to 0. It is evident that M1 cannot be used for EAS simulation due to its negative values. These values indicate that during the relaxation process, the stress not only decreases but also changes direction. For instance, if there were a relaxation test with initial compression, a negative relaxation modulus would mean that the compressive stress would not only decrease but also become tensile stress afterward. It should be noted that such a problem with M1 has already been indicated in Bažant and Jirásek (2018), suggesting that the high nonlinearity of the relaxation modulus results in underestimating the relaxation modulus by numerical solutions. Therefore, instead of the initial conditions as in Equation (9), Bažant and Jirásek (2018) proposed an empirical solution by using the initial conditions as in Equation (10) to ease problems in the conversion of relaxation modulus of later ages (several days to weeks). However, despite the improvement brought by Equation (10), it is shown here that the negative relaxation modulus still exists (Figure 13a,c), which indicates that M1 needs further improvement probably in numerical schemes before it can be used appropriately to simulate stress relaxation in very early age cementitious materials (from several hours to a week in this study).

In fact, the negative relaxation modulus (caused by M1) mainly results from the rapid decrease of the creep compliance function due to the aging term (specifically, term $(1/t_0)^b$ in Equations 25 and 26). This becomes evident when assuming that concrete creep is not subject to aging (by omitting the aging term) and then recalculating the relaxation modulus using M1 as depicted in Figure 14a. When the load is applied at intervals of 10, 20, …, up to 160 h, over a total timeframe of 1000 h, the issue of the negative

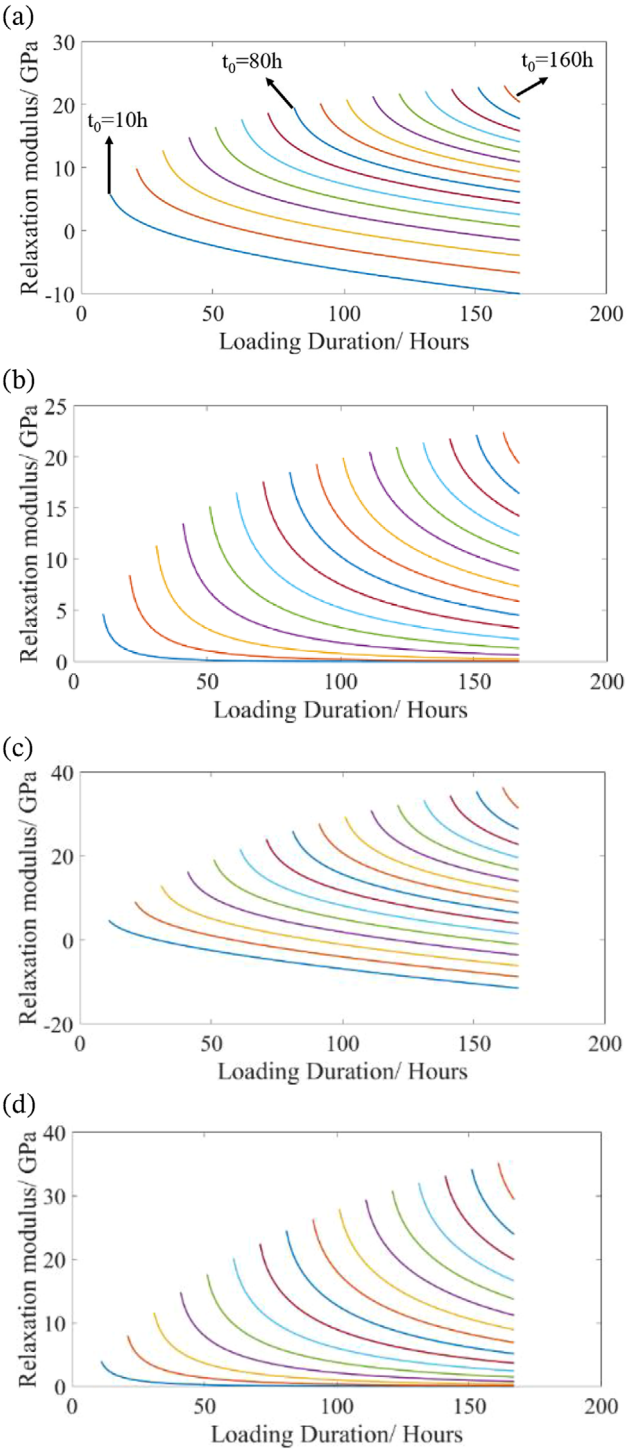

FIGURE 13 Relaxation modulus $R\ (t_0,\ t)$: (a) C1 results by M1, (b) C1 results by M2, (c) C3 results by M1, and (d) C3 results by M2. (Note that the results displayed here are $R\ (t_0,\ t)$ with t_0 equal to 10, 20, 30, …, and 160 h. See (a) for the example.)

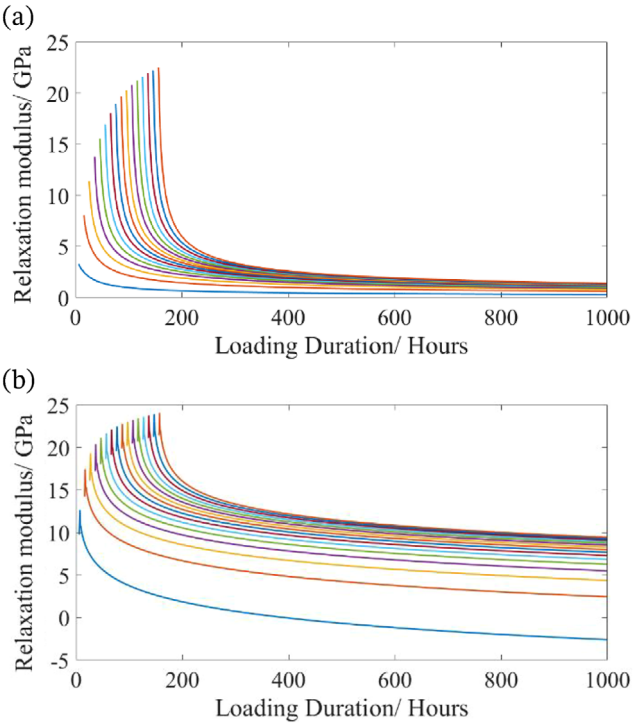

FIGURE 14 Relaxation modulus $R(t_0, t)$ converted from creep compliance function by M1 for: (a) C1 creep compliance function with a constant aging term; (b) ACI-based creep compliance function for normal concrete as used in Yu et al. (2012). (Note that the results displayed here are $R(t_0, t)$ with t_0 equals 10, 20, 30, …, and 160 h. See Figure 13a for the example.)

relaxation modulus completely disappears. Additionally, employing a creep compliance function for regular concrete, which is typically recommended for long-term creep analysis by many design codes, also solves the issue of negative relaxation modulus. For instance, by applying the creep compliance function from the ACI code, with parameters equivalent to those described in Equation (27) for concrete (Yu et al., 2012), the relaxation modulus following M1 can be calculated as shown in Figure 14b. The negative relaxation modulus is only observed at the very beginning. Consequently, the negative relaxation modulus problem induced by M1 primarily occurs in very early-age materials with high creep. For long-term creep analyses, such concerns regarding M1 are likely negligible.

$$E(t_0) = 38000 * \left(e^{0.2 * \left(1 - \sqrt{\frac{28}{t_0}}\right)} \right)^{0.3} \tag{27.1}$$

$$\varphi(t_0, t) = 2 * (1.25 * t_0)^{-0.118} * (t - t_0)^{0.2} \tag{27.2}$$

$$J(t_0, t) = \frac{1 + \varphi(t_0, t)}{E(t_0)} \tag{27.3}$$

4.2.2 | The integral check

The integral check is performed here by substituting the converted relaxation modulus (obtained by M1 and M2) and creep compliance function (i.e., Equations 25 and 26) into Equation (8) and checking if the integral still equals 1.0. To evaluate the difference between the integral value of Equation (8) and the theoretical value (i.e., 1), the root mean square error (RMSE) index is here used. It can be expressed as

$$RMSE = \sqrt{\frac{\sum_N (y_c - y_r)^2}{N}} \tag{28}$$

where y_c is the calculated value of the integral expression in Equation (8) at different t and t_0; y_r is the value that the integral in Equation (8) must have, that is, 1; N is the amount of the considered points, and in this case, it is $N = t_0 * t$. The integral check results for the converted relaxation modulus of both pastes obtained by M1 and M2 are shown in Figure 15. The results of the integral check for t = 20:168 and t_0 = 1:168 are shown. To present the overall shape of the relaxation function, the results in the very beginning (i.e., t = 1:20) are not shown. However, it should be noted that the RMSEs in each result were calculated based on all the t_0 and t. The integral check results clearly show that the relaxation modulus converted by the M1 (Figure 15a,c) has a much lower RMSE (around 0.10) than the relaxation modulus converted by the M2 (Figure 15b,d), which obtained a higher RMSE around 0.43.

Such results are understandable if one checks the detail of the M1 and M2: M1 (Equations 9 and 10) is basically another form of numerical solution of the integral check (Equation 7), and therefore M1 naturally satisfies the criterion that the integral value calculated by Equation (8) should equal to 1.0. The RMSE of approximately 0.1 is just the accuracy loss of the adopted numerical scheme (i.e., mid-point rule). However, on the other hand, it should be noted that the derivation of M2 (Equations 11–16) does not have any prior information regarding the integral. Thus, it obtains a higher RMSE of about 0.43. Specifically, looking at Figure 15b,d, it is found that the error of M2 in integral check tends to be higher, especially at a very early age (i.e., at small t_0). Note that the problem of negative values of relaxation modulus obtained by M1 (Figure 13a,c) also tends to be more significant at a very early age (i.e., at small t_0). Considering all the negative values in Figure 13a,c as mere errors of adopted numerical schemes, one can correct all negative values to zero and do the integral check again with the adjusted relaxation modulus. The results of the relaxation modulus obtained by such adjusted M2 are shown in Figure 16. It is interesting to see that, after correcting all the negative values to 0, the adjusted M1 obtains

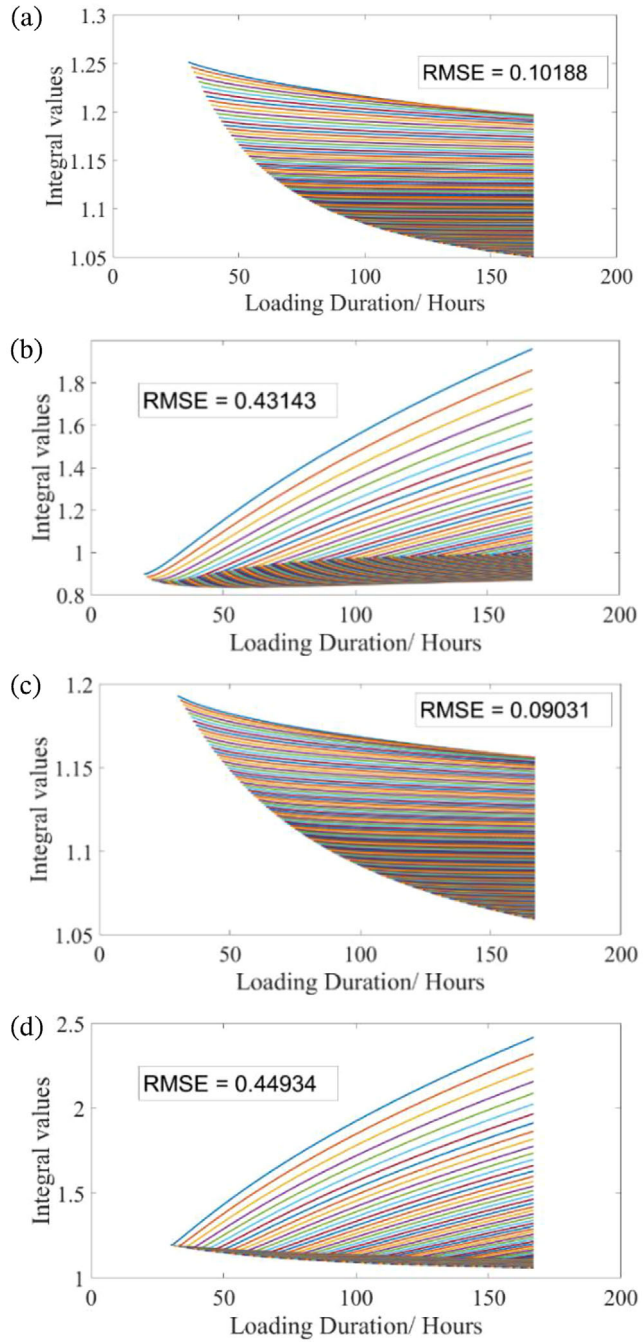

FIGURE 15 Integral values given by Equation (8) using converted relaxation modulus and tested creep compliance function as input: (a) C1 results converted by M1, (b) C1 results converted by M2, (c) C3 results converted by M1, (d) C3 results converted by M2. (Note that the results displayed here are integral values of Equation 8 with t and t_0 equal to 1, 2, 3, …, 168 h.)

a similar RMSE with M2. Moreover, the error distribution of the adjusted M1 is also similar to that of M2: earlier ages tend to have higher RMSE and, therefore, more deviation from the criterion of integral check.

From the result analysis of this section, it is found that despite M1 satisfying the integral check with better accuracy with a low RMSE of around 0.10, it obtains negative values of relaxation modulus, especially in early age, which is due to the high nonlinearity of relaxation modulus function at the beginning according to Bažant and Jirásek (2018). In comparison, M2 does not lead to negative values but only a smooth convergence to 0. Negative values of the relaxation modulus indicate an unacceptable stress relaxation process that may not be suitable for simulating stress relaxation in early-age cementitious materials. Considering the negative values in M1 as numerical loss and correcting them to zero, the obtained RMSE in the integral check is similar to M2, which is around 0.40.

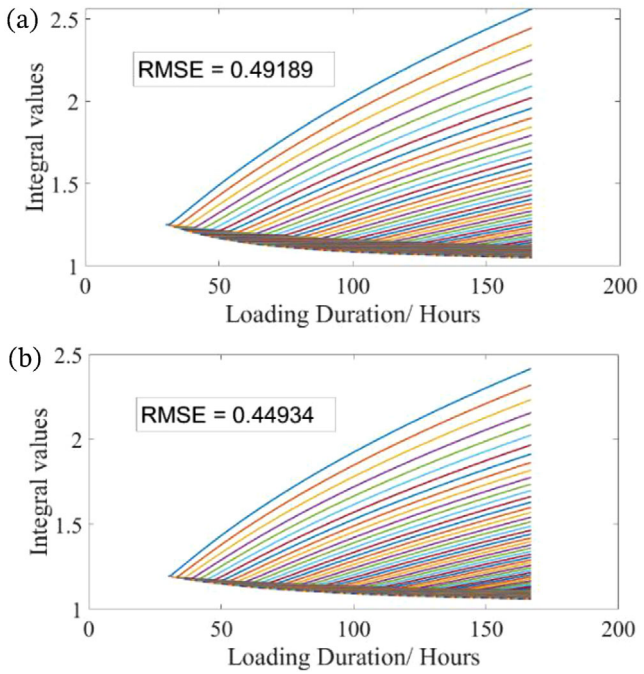

FIGURE 16 Integral values given by Equation (8) using adjusted M1 by setting all negative values to 0: (a) C1 results and (b) C3 results.

4.3 | The 3D analysis based on exponential algorithms (checkpoints 1 and 2)

The 3D analysis implements M3 and M4 in FEM, extensions of the 1D method M1 and M2. The exponential algorithm solves the Volterra integral (Equations 4 and 6) with a quasi-elastic constitutive relationship (Equation 17), which is more efficient than directly solving the integral with classical numerical schemes and, therefore, is more suitable in simulating viscoelastic behavior in massive structures, including the EAS prediction. In this section, virtual creep and relaxation tests will be done using the M3 and M4, respectively, to illustrate the applicability of the

exponential algorithm based on either Kelvin or Maxwell chain in simulating the viscoelastic behavior of very early-age cementitious materials. Specifically, checkpoints 1 and 2 in Figures 7 and 9 will be examined in this section for both M3 and M4. All the virtual tests will be conducted at four different ages, including 7, 24, 48, and 72 h.

4.3.1 | Kelvin chain

The M3 is the exponential algorithm based on the Kelvin chain model. The spectrum of the Kelvin chain was fitted using the continuous retardation chain method (Equation 22) based on the experimental results of the creep compliance function (Equations 25 and 26). Checkpoint 1 of M3 aims to conduct a virtual uniaxial creep test on the prism (Figure 5a) and compare the obtained creep compliance function from such tests with the experimental results (i.e., the input for the Kelvin chain). The results of checkpoint 1 of M3 are shown in Figure 17. The results of checkpoint 1 indicate that the M3 can almost perfectly simulate the creep test given a specific input, meaning high precision is achieved by the exponential algorithm based on the Kelvin chain to calculate the Volterra integral (Equations 4 and 6). However, this suggests that similar problems of negative relaxation modulus happening to M1 will also occur in M3 if it comes to the conversion from creep to relaxation. As shown in Figure 18, the relaxation modulus can be obtained by applying a constant displacement on the prism. The relaxation modulus converted by M1 and M2 are also compared. The results of the virtual relaxation tests conducted by M3 show a similar non-converging trend as observed in the results of M1. This non-converging trend leads to a negative relaxation modulus, indicating a problematic stress direction change in the relaxation process. Such a result is unacceptable for EAS simulation.

4.3.2 | Maxwell chain

Compared to the Kelvin chain, the Maxwell chain is often less used because it is difficult to obtain the relaxation modulus, which the Maxwell chain requires as the input. In this study, we first used the M2 to convert the creep compliance function obtained from the hourly repeated loading test to the relaxation modulus. Then, a non-linear optimizer was employed to fit a 13-unit Maxwell chain using the relaxation modulus obtained by M2. The obtained spectrum of the Maxwell chain for the two cementitious materials CEM I/42.5N and CEM III/B 42.5N with a w/c ratio of 0.30 are shown in Figure 19. Note that the Maxwell spectrum is a 168×13 array, with the first axis being the investigated time ranging from 1 to 168 h and the second axis being the 13 different Maxwell units with relaxation time logarithmically distributed from 10^{-6} to 10^{6} h. The values in the array are the ratio between the elastic modulus of the spring in the unit and the elastic modulus of the cement paste material.

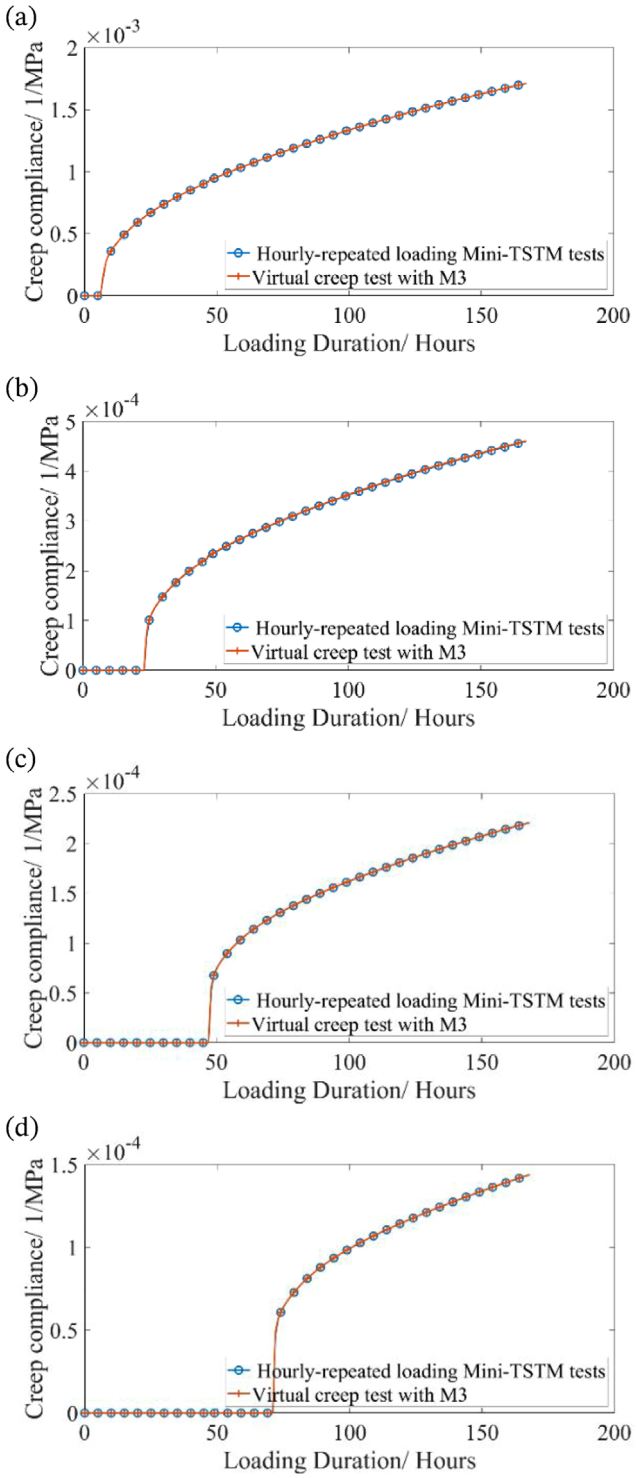

FIGURE 17 Creep compliance obtained from virtual creep test of M3 (checkpoint 1), with loading time $t_0 = 7$, 24, 48, and 72 h for (a–d), respectively.

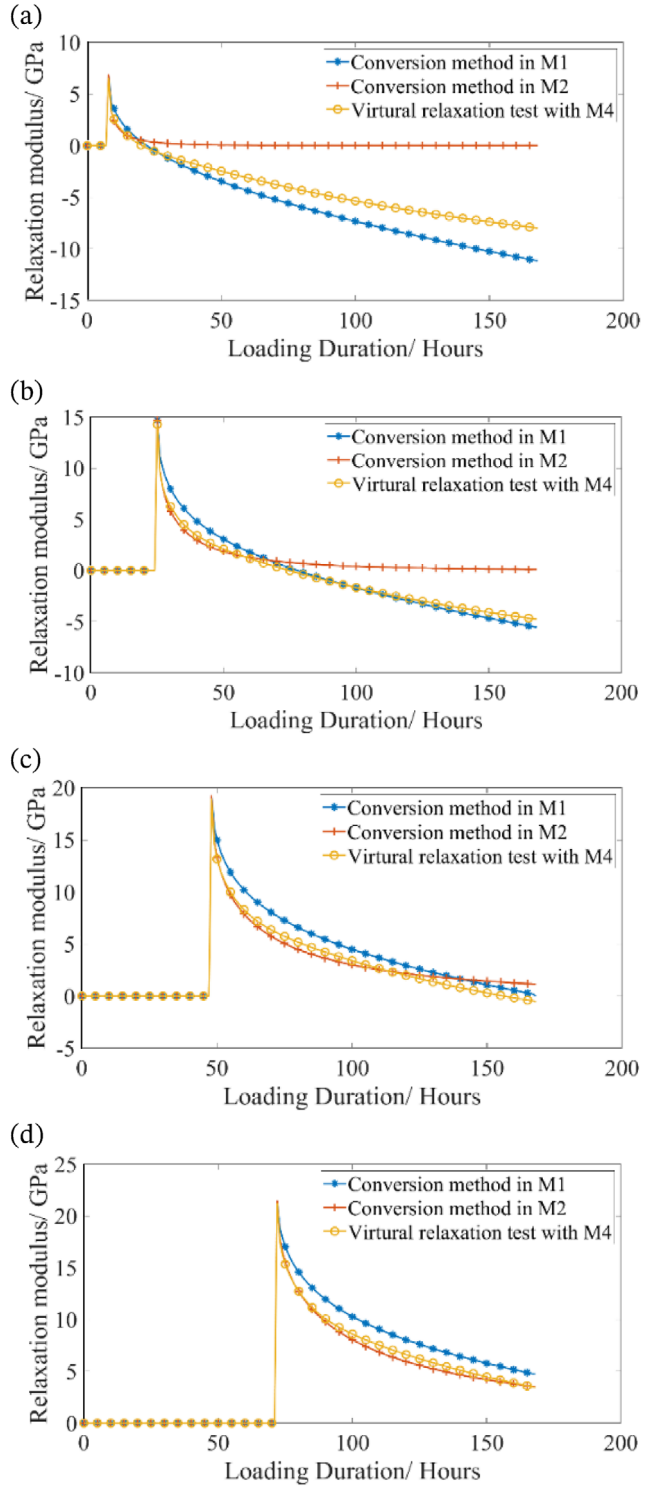

FIGURE 18 Relaxation modulus obtained from the virtual creep test of M3 (checkpoint 1), with loading time t_0 = 7, 24, 48, and 72 h for (a–d), respectively.

The relaxation modulus can be obtained by applying a constant unit displacement on the top of the prism, which can then be compared to the input of the adopted Maxwell chain model (i.e., checkpoint 1). The relaxation modulus in the virtual relaxation test can be shown in

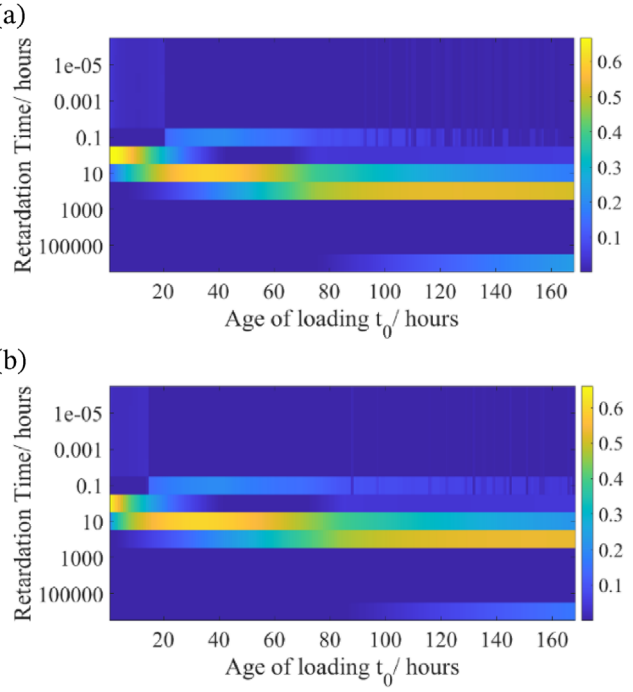

FIGURE 19 Spectrum of the Maxwell chain model of two types of adopted cementitious materials: (a) CEM I/42.5N and (b) CEM III/B 42.5N. (Note the y-axis is the retardation time μ_j of jth unit and can be calculated by $\mu_j = \eta_j/E_j$.)

Figure 20. The relaxation modulus obtained by M1 and M2 are also compared. From the perfect match between the relaxation modulus obtained by M4 and M2, it is clear that the exponential algorithm based on the Maxwell chain can simulate the relaxation behavior with good precision, indicating the applicability of M4 in EAS simulation. By applying a constant unit load on top of the prism, virtual creep tests can be done, and checkpoint 2 can be examined as shown in Figure 21. If M2 can perfectly reflect the coupling between creep and relaxation, then the obtained creep compliance in the virtual creep test should match the experimental results. However, the results of checkpoint 2 in Figure 21 clearly show that at an early age, the creep compliance function obtained by M4 (calibrated based on the input of M2) does not match the experimental creep results. However, at a later age, the difference becomes smaller. At 72 h, the two creep compliance curves become very similar. Such a pattern has been shown in the integral check of M2, in which the integral values are far from 1.0 if at an earlier age, and vice versa. Since M4 is calibrated by the relaxation modulus of M2, a similarly weak coupling between creep and relaxation like M2 at a very early age can also be understandable.

Overall, this section found that given the input of the creep compliance function or relaxation modulus function, M3 and M4 can perfectly simulate the creep and relaxation behavior with high precision, respectively.

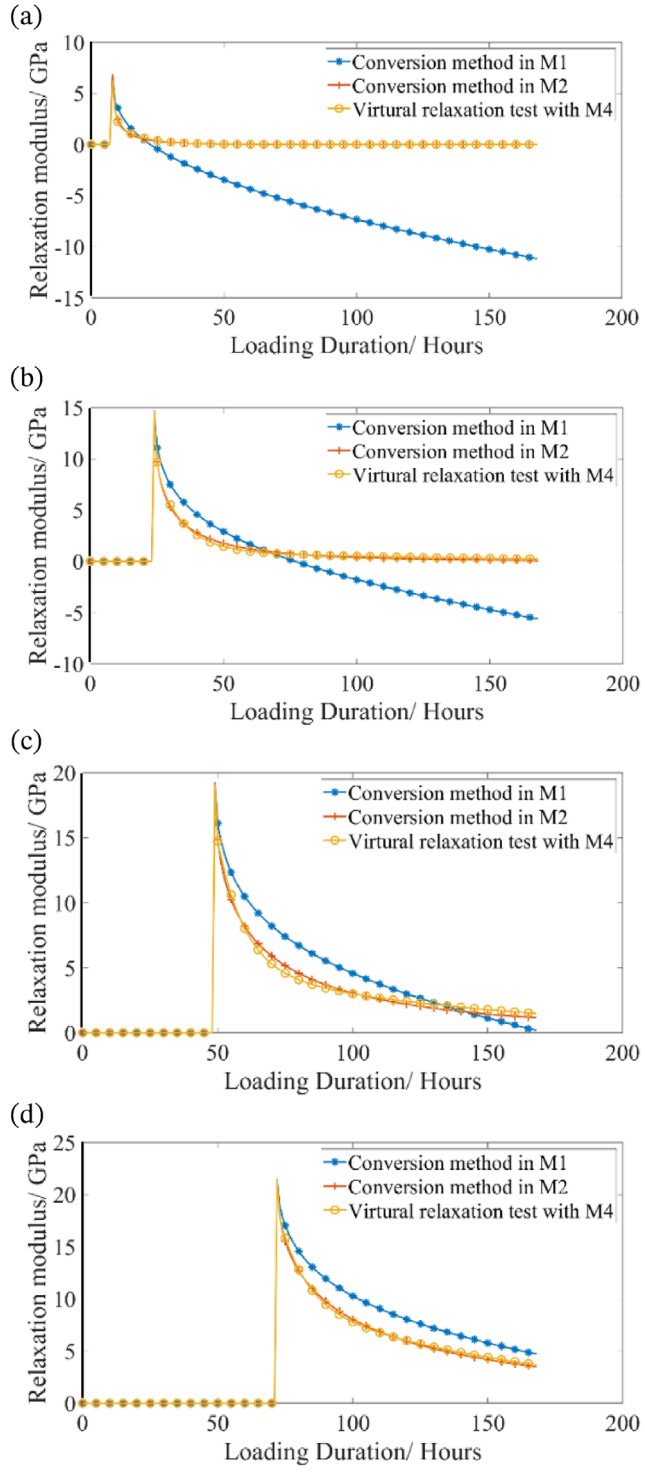

FIGURE 20 Relaxation modulus obtained from virtual relaxation test of M4 (checkpoint 1), with time of loading t_0 = 7, 24, 48, and 72 h for (a–d), respectively.

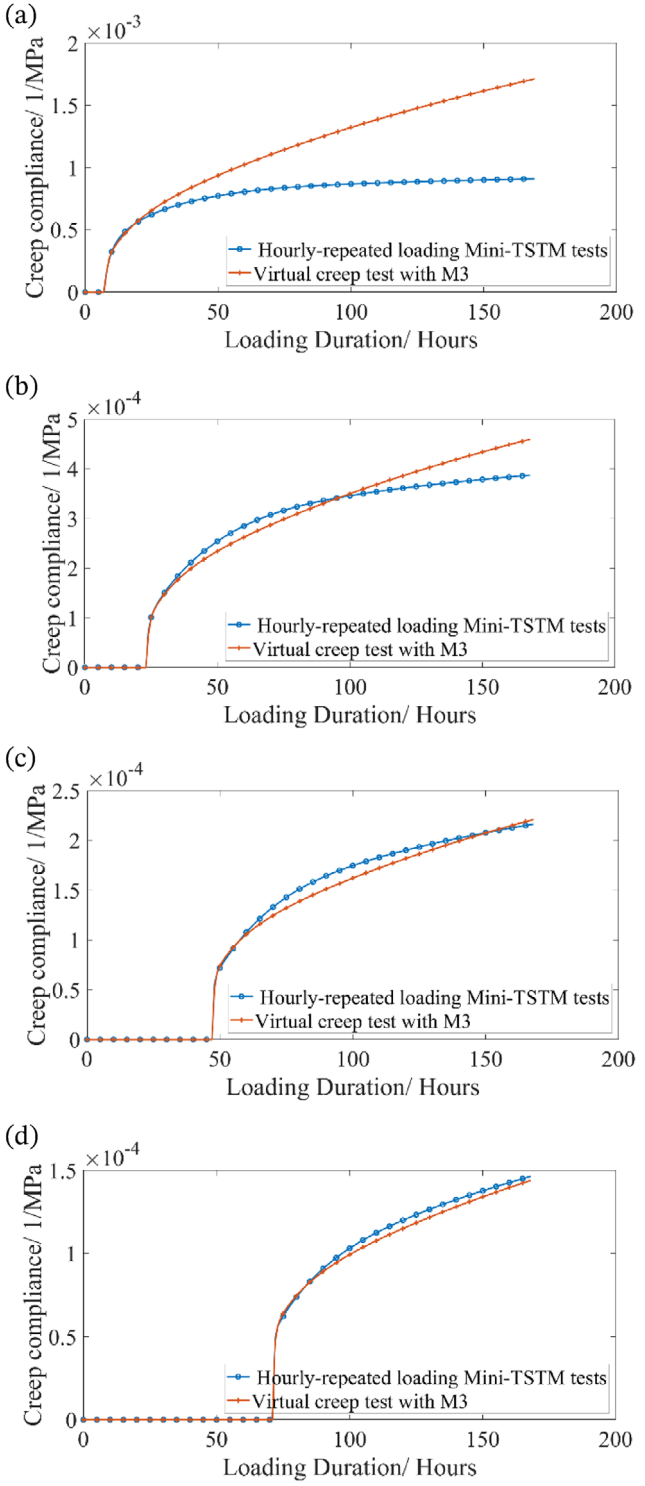

FIGURE 21 Creep compliance obtained from virtual relaxation test of M4 (checkpoint 2), with a loading time t_0 = 7, 24, 48, and 72 h for (a–d), respectively.

However, M3 and M4 cannot reflect the coupling between creep and relaxation well. In M3, given the creep compliance function as input, the relaxation modulus obtained from a virtual relaxation test can be negative, especially when the loading time t_0 is small. Such a problem is similar to M1 and is understandable since M1 and M3 are based on the same original Volterra integral (Equation 6). To simulate EAS, a negative relaxation modulus is not physically acceptable because it conveys a problematic relaxation process with a change of stress sign. On the

other hand, using the relaxation modulus obtained by M2 as input for the M4, a more reasonable relaxation modulus can be obtained in the virtual relaxation test, which always converges to 0. However, a weaker coupling between creep and relaxation still exists at a very early age (as observed in the integral check of M2).

4.4 | Prediction of EAS (checkpoint 3)

In this section, the M1–M4 will be used to predict the EAS using the AD in Figure 10b,d and measured viscoelastic properties in Equations (25) and (26) as input. The predicted EAS can then be compared to the experimental results in Figure 10a,c. Data are from six testing results (three for CEM I 42.5/N and three for CEM III/B 42.5/N). Precisely, for 1D analysis methods M1 and M2, the prediction of EAS was calculated based on Equation (5), using the relaxation modulus given by Equations (9) and (10) and Equation (16), respectively. For 3D analysis methods M3 and M4, the prediction of EAS was simulated based on the dog-bone specimen with two ends fixed, similar to the Mini-TSTM test (Figure 5b). The exponential algorithm based on Kelvin and Maxwell chains was implemented based on Equations (17) and (19) and Equations (17) and (24), respectively. The experimental and numerical results of EAS are shown in Figure 22. To display the difference between the experimental and numerical results, the RMSE was calculated based on Equation (27). Note that for M1, there are four different variants:

1. M1: Original M1, based only on Equation (9).
2. M1-zeroed: Adjusted M1, which sets all negative relaxation modulus obtained by M1 as 0.
3. M1-2: Improved M1, based on Equations (9) and (10). The initial condition changes in Equation (10) mainly aim to reduce the error of high nonlinearity of the relaxation modulus function (Bažant & Jirásek, 2018).
4. M1-2-zeroed: Adjusted M1-2 sets negative relaxation modulus obtained by M1-2 as 0.

Figure 22 shows only the original and adjusted M1 for clarity. But RMSEs of all studied methods are shown in the Table 2. Comparing the averaged RMSEs of all models, the rank of prediction accuracy is as follows: M2 (0.265) < M4 (0.300) < M1-2-Zeroed (0.302) < M1-Zeroed (0.395) < M1-2 (0.520) < M1 (0.752) < M3 (0.783). The following analysis can be drawn:

1. The models M2 and M4 both obtain high accuracy with a low averaged RMSE below 0.300 MPa. Note that M4 is the FEM model that can be generalized to 3D analysis of a more realistic structure. At the same time, M2 is a simple model for 1D analysis, such as the uniaxial restraint test in this study. A similar accuracy of M2 and M4 is expected because M4 uses the relaxation modulus derived from M2 to calibrate the spectrum of the Maxwell chain. The high prediction accuracy given by M2 and M4 also shows that, in the results of Mini-TSTM and Mini-ADTM tests (Figure 10), each AD is an exclusive description of the corresponding EAS results, which verifies the variation of AD between different batches of cement.
2. The models M1 and M3 obtain the highest RMSE and, therefore, the lowest accuracy of EAS prediction. This result is expected if considering the influence of high nonlinearity of the relaxation function (Bažant & Jirásek, 2018), which causes an underestimation of relaxation modulus calculation if strictly following Equation (9) for the conversion. The similar performance of M1 and M3 is expected because both are based on the same governing equation: M3 employs the exponential algorithm using the Kelvin chain by Equations (17) and (19), which is initially derived by the incremental form of Equation (6), and Equation (6) is also the basis of Equation (9) for M1.
3. The negative values of relaxation modulus and error brought by the high nonlinearity of the relaxation function in the conversion process are mainly responsible for why a worse prediction is obtained: By correcting all the negative relaxation modulus to 0, the prediction accuracy is significantly improved, which can be seen by comparing the RMSE of M1 to M1-zeroed and M1-2 to M1-2-zeroed. By reducing the error brought by the high nonlinearity of the relaxation function using Equation (10), the prediction accuracy is also improved, which can be seen by comparing the RMSE of M1 to M1-2 and M1-zeroed to M1-2-zeroed. If correcting both, the adjusted M1-2-zeroed can obtain comparable accuracy to M2 and M4, which brings a low averaged RMSE of around 0.302 MPa.
4. However, it should be noted that simply correcting all negative values to zero or applying a different initial condition (as in Equation 10) may not intrinsically solve the numerical issue induced by the high nonlinearity of the relaxation function. And therefore, such improvement cannot be directly extended to 3D models (i.e., M3). Improvements are needed for better application of M3 in EAS analysis, considering the high nonlinearity of relaxation functions. Alternatively, this study proves that the M4 model, which uses the relaxation modulus from M2 as input, is well applicable in EAS simulation.

Overall, the analysis above proves that the M4, based on the aging Maxwell chain, exponential algorithm, and the exponential conversion from creep to relaxation, can well

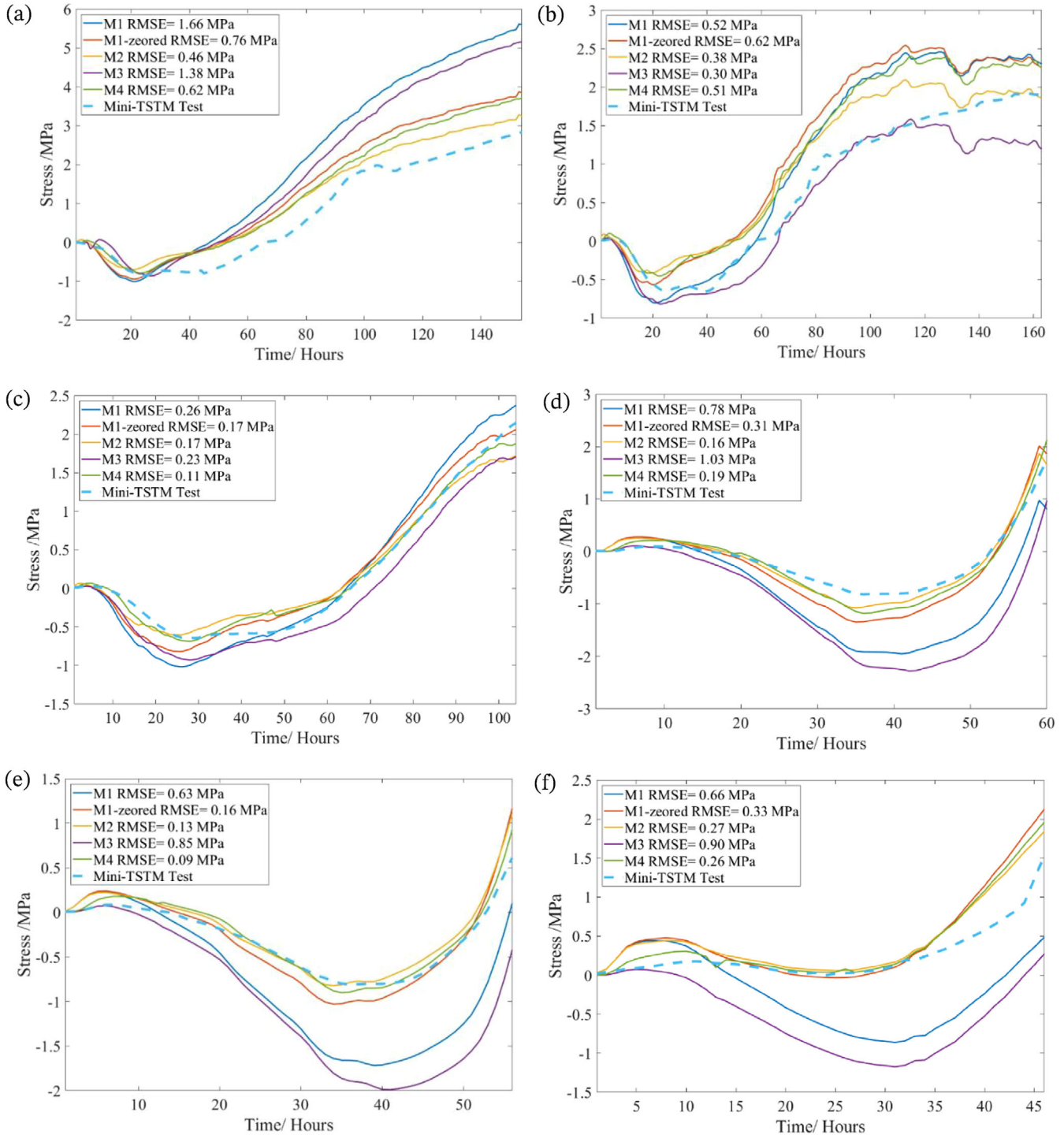

FIGURE 22 Experimental and numerical results of EAS, Fig (a–f) correspond to results of C1-30-1, C1-30-2, C1-30-3, C3-30-1, C3-30-2, C3-30-3, respectively.

address the problem of negative relaxation modulus and high non-linearity as brought by M1 and M3, and therefore significantly improves the EAS prediction accuracy. Although the EAS can be well quantified through M3, the EAC criterion is equally important to fully assess EAC risk. A straightforward assessment criterion is the stress-nominal strength ratio. Many studies (Xin et al., 2020) on TSTM tests showed that EAC always happens before the stress-nominal strength ratio reaches 1.0 and mostly between 0.60 and 0.80. Therefore, engineering practice often uses a stress-nominal strength ratio of 0.5. A more sophisticated damage criterion may be needed to assess the EAC risk precisely, such as a combination of the EAS and strain (Zhu et al., 2021).

TABLE 2 Root mean square error between predicted and tested early-age stress.

	M1	M1-zeroed	M1-2	M1-2-zeroed	M2	M3	M4
C1-30-1	1.66	0.76	1.20	0.59	0.46	1.38	0.62
C1-30-2	0.52	0.62	0.49	0.49	0.38	0.30	0.51
C1-30-3	0.26	0.17	0.17	0.15	0.17	0.24	0.11
C3-30-1	0.78	0.31	0.50	0.18	0.16	1.03	0.19
C3-30-2	0.63	0.18	0.35	0.14	0.15	0.85	0.10
C3-30-3	0.66	0.33	0.41	0.26	0.27	0.90	0.26
Average	0.751	0.396	0.520	0.301	0.264	0.783	0.299

Moreover, it should be noted that the models M1–M4 are built based on the Boltzmann superposition (as Equation 3), which assumes that the EAS induced at every time point is additive. However, this assumption may be invalid and affect EAS prediction accuracy when stress is close to its strength. Finally, it should be mentioned that in this work, the EAS caused by AD is used as an example. The calculation methods also hold for the EAS caused by thermal and drying deformation since the imposed deformation in Equation (4) does not refer to a specific type of deformation.

5 | CONCLUSION

This study investigated four different numerical approaches (two for 1D analysis and another two for 3D analysis) for simulating the EAS evolution in cementitious materials. Based on the experimental results of a newly developed Mini-TSTM and Mini-ADTM, the AD and viscoelastic properties (i.e., elastic modulus and aging creep) were measured and served as input for the EAS simulation. The EAS of two different cement pastes (i.e., CEM I 42.5N and CEM III/B 42.5N) were also tested by the Mini-TSTM to evaluate the modeling accuracy. The paper comprehensively introduces and analyzes numerical models M1 to M4, including their theoretical foundations, applications, and validation. M1 and M2 are 1D solutions for converting the creep to relaxation, with M1 being the numerical solution from the Volterra integral as Equation (9) and M2 being an explicit exponential conversion function as Equation (16). M3 and M4 are developed for simulating both creep and relaxation behaviors of concrete in 3D using FEM, using rate-type creep law with Kelvin chain as Equations (18)–(22) and Maxwell chain as Equations (23) and (24). Based on this study, the following conclusions can be drawn:

1. As the numerical solution of the Volterra integral (Equation 6), the 1D model M1 and 3D model M3 both lead to negative relaxation modulus in a similar manner, which indicates a problematic change of stress sign in the relaxation process. This is not physically justified and suggests that the M1 and M3 can induce some errors when simulating EAS. As expected, in the EAS comparison, M1 and M3 were proved to show the highest error. However, it should be noted that the negative issue of M1 is mainly induced by fast aging at a very early age. Such negative issues can be neglected for mature material or long-term creep/relaxation analysis.
2. Derived by the definition of a relaxation test, the exponential conversion function of M2 can provide reasonable relaxation modulus using the measured viscoelastic properties as input. The 1D model M2 obtained the highest accuracy in EAS prediction among all investigated models. To generalize into 3D, a FEM model with the exponential algorithm based on the Maxwell chain (i.e., M3) was developed, which takes the relaxation modulus of M2 as input and obtains good prediction accuracy of EAS in 3D analysis that is comparable to M2.
3. The relaxation modulus function's high nonlinearity is one reason for the negative relaxation modulus. By correcting the negative relaxation modulus to zero and using a different initial condition (Equation 10), the error brought by such non-linearity can be eased, and good prediction accuracy of EAS can be obtained (see the prediction performance of M1-2-Zeroed in Section 4.4).
4. The models developed (M1-2-Zeroed, M2, and M4) can accurately predict the EAS despite the apparent variations in the AD of the same type of cement. These models use the AD from the same testing batch of EAS as input, indicating a consistency between the AD and EAS within the same batch. However, using the AD from one testing batch to predict the EAS of another batch may lead to a decrease in accuracy due to variations in AD between different testing batches. Therefore, each AD is a unique description of the corresponding EAS evolution.
5. The prediction of EAS plays a crucial role in determining EAC criteria, such as the maximum stress-strength

ratio (typically limited to 0.50 in practical applications). To establish more accurate damage criteria for EAC risk assessment, both EAS and strain need to be considered. For a high stress-strength ratio, a numerical model requires a comprehensive constitutive law to account for the aging fracture properties of the material. However, this is beyond the scope of the present paper.

ACKNOWLEDGMENTS

Minfei Liang would like to acknowledge the funding support provided by the China Scholarship Council under Grant Number 202007000027. Branko Šavija acknowledges the financial support of the European Research Council (ERC) within the framework of the ERC Starting Grant Project "Auxetic Cementitious Composites by 3D printing (ACC-3D)," Grant Agreement Number 101041342. The codes and data used in this study are available upon request.

REFERENCES

Alnaggar, M., Di Luzio, G., & Cusatis, G. (2017). Modeling time-dependent behavior of concrete affected by alkali silica reaction in variable environmental conditions. *Materials*, *10*(5), 471. https://doi.org/10.3390/ma10050471

American Concrete Institute., & ACI Committee 209–Creep and Shrinkage. (2008). Guide for modeling and calculating shrinkage and creep in hardened concrete. *American Concrete Institute*.

Azenha, M., Kanavaris, F., Schlicke, D., Jędrzejewska, A., Benboudjema, F., Honorio, T., Šmilauer, V., Serra, C., Forth, J., Riding, K., Khadka, B., Sousa, C., Briffaut, M., Lacarrière, L., Koenders, E., Kanstad, T., Klausen, A., Torrenti, J. M., & Fairbairn, E. M. R. (2021). Recommendations of RILEM TC 287-CCS: Thermo-chemo-mechanical modelling of massive concrete structures towards cracking risk assessment. *Materials and Structures/Materiaux et Constructions*, *54*(4), 135. https://doi.org/10.1617/s11527-021-01732-8

Baronet, J., Sorelli, L., Charron, J. P., Vandamme, M., & Sanahuja, J. (2022). A two-scale method to rapidly characterize the logarithmic basic creep of concrete by coupling microindentation and uniaxial compression creep test. *Cement and Concrete Composites*, *125*, 104274. https://doi.org/10.1016/j.cemconcomp.2021.104274

Bažant, Z. P., & Baweja, S. (1994). Creep and shrinkage prediction model for analysis and design of concrete structures—Model B3. Structural Engineering Report 94-10/603 c (Northwestern University).

Bažant, Z. P., & Jirásek, M. (2018). Creep and hygrothermal effects in concrete structures *(Vol. 225)*. Springer. https://doi.org/10.1007/978-94-024-1138-6

Bazant, Z. P., & Osman, E. (1976). Double power law for basic creep of concrete. *Matériaux et Construction*, *9*(1), 3–11.

Bažant, Z. P., & Wu, S. T. (1974). Rate-type creep law of aging concrete based on maxwell chain. *Matériaux et Constructions*, *7*(1), 45–60. https://doi.org/10.1007/BF02482679

Bažant, Z. P., & Xi, Y. (1995). Continuous retardation spectrum for solidification theory of concrete creep. *Journal of Engineering Mechanics*, *121*(2), 281–288. https://doi.org/10.1061/(ASCE)0733-9399(1995)121:2(281)

Beltempo, A., Bursi, O. S., Cappello, C., Zonta, D., & Zingales, M. (2018). A viscoelastic model for the long-term deflection of segmental prestressed box girders. *Computer-Aided Civil and Infrastructure Engineering*, *33*(1), 64–78. https://doi.org/10.1111/mice.12311

Bendimerad, A. Z., Delsaute, B., Rozière, E., Staquet, S., & Loukili, A. (2020). Advanced techniques for the study of shrinkage-induced cracking of concrete with recycled aggregates at early age. *Construction and Building Materials*, *233*, 117340. https://doi.org/10.1016/j.conbuildmat.2019.117340

Bentur, A., Igarashi, S., & Kovler, K. (2001). Prevention of autogenous shrinkage in high-strength concrete by internal curing using wet lightweight aggregates. *Cement and Concrete Research*, *31*(11), 1587–1591. https://doi.org/10.1016/S0008-8846(01)00608-1

Bjøntegaard, Ø. (1999). *Thermal dilation and autogenous deformation as driving forces to self-induced stresses in high high-performance concrete* [Doctoral dissertation, Norwegian University of Science and Technology (NTNU)].

Briffaut, M., Benboudjema, F., & D'Aloia, L. (2016). Effect of fibres on early age cracking of concrete tunnel lining. Part I: Laboratory ring test. *Tunnelling and Underground Space Technology*, *59*, 215–220. https://doi.org/10.1016/J.TUST.2016.07.016

Byrd, R. H., Gilbert, J. C., & Nocedal, J. (2000). A trust region method based on interior point techniques for nonlinear programming. *Mathematical Programming*, *89*(1), 149–185. https://doi.org/10.1007/PL00011391

Byrd, R. H., Hribar, M. E., & Nocedal, J. (1999). An interior point algorithm for large-scale nonlinear programming. *SIAM Journal on Optimization*, *9*(4), 877–900. https://doi.org/10.1137/S1052623497325107

Carette, J., & Staquet, S. (2018). Unified modelling of the temperature effect on the autogenous deformations of cement-based materials. *Cement and Concrete Composites*, *94*, 62–71. https://doi.org/10.1016/j.cemconcomp.2018.08.008

Cibelli, A., Pathirage, M., Cusatis, G., Ferrara, L., & Di Luzio, G. (2022). A discrete numerical model for the effects of crack healing on the behaviour of ordinary plain concrete: Implementation, calibration, and validation. *Engineering Fracture Mechanics*, *263*, 108266. https://doi.org/10.1016/j.engfracmech.2022.108266

Coleman, T. F., & Li, Y. (1994). On the convergence of interior-reflective Newton methods for nonlinear minimization subject to bounds. *Mathematical Programming*, *67*(1-3), 189–224. https://doi.org/10.1007/BF01582221

Coleman, T. F., & Li, Y. (1996). An interior trust region approach for nonlinear minimization subject to bounds. *SIAM Journal on Optimization*, *6*(2), 418–445. https://doi.org/10.1137/0806023

Darquennes, A., Staquet, S., & Espion, B. (2011). Behaviour of slag cement concrete under restraint conditions. *European Journal of Environmental and Civil Engineering*, *15*(5), 787–798. https://doi.org/10.1080/19648189.2011.9693365

Delsaute, B., Boulay, C., & Staquet, S. (2016). Creep testing of concrete since setting time by means of permanent and repeated minute-long loadings. *Cement and Concrete Composites*, *73*, 75–88. https://doi.org/10.1016/J.CEMCONCOMP.2016.07.005

Destrebecq, J., & Jurkiewiez, B. (2001). A numerical method for the analysis of rheologic effects in concrete bridges. *Computer-Aided*

Civil and Infrastructure Engineering, *16*(5), 347–364. https://doi.org/10.1111/0885-9507.00238

Di Luzio, G., Cedolin, L., & Beltrami, C. (2020). Tridimensional long-term finite element analysis of reinforced concrete structures with rate-type creep approach. *Applied Sciences*, *10*(14), 4772. https://doi.org/10.3390/app10144772

Di Luzio, G., & Cusatis, G. (2013). Solidification–microprestress–microplane (SMM) theory for concrete at early age: Theory, validation and application. *International Journal of Solids and Structures*, *50*(6), 957–975. https://doi.org/10.1016/J.IJSOLSTR.2012.11.022

Gan, Y., Romero Rodriguez, C., Zhang, H., Schlangen, E., van Breugel, K., & Šavija, B. (2021). Modeling of microstructural effects on the creep of hardened cement paste using an experimentally informed lattice model. *Computer-Aided Civil and Infrastructure Engineering*, *36*(5), 560–576. https://doi.org/10.1111/mice.12659

Gan, Y., Vandamme, M., Zhang, H., Chen, Y., Schlangen, E., van Breugel, K., & Šavija, B. (2020). Micro-cantilever testing on the short-term creep behaviour of cement paste at micro-scale. *Cement and Concrete Research*, *134*, 106105. https://doi.org/10.1016/j.cemconres.2020.106105

Gill, P. E., Murray, W., & Wright, M. H. (1981). *Practical optimization*. Academic Press.

Han, S. P. (1977). A globally convergent method for nonlinear programming. *Journal of Optimization Theory and Applications*, *22*(3), 297–309. https://doi.org/10.1007/BF00932858

Igarashi, S., Bentur, A., & Kovler, K. (2000). Autogenous shrinkage and induced restraining stresses in high-strength concretes. *Cement and Concrete Research*, *30*(11), 1701–1707. https://doi.org/10.1016/S0008-8846(00)00399-9

Irfan-ul-Hassan, M., Pichler, B., Reihsner, R., & Hellmich, Ch. (2016). Elastic and creep properties of young cement paste, as determined from hourly repeated minute-long quasi-static tests. *Cement and Concrete Research*, *82*, 36–49. https://doi.org/10.1016/j.cemconres.2015.11.007

Ji, G. M., Kanstad, T., & Bjøntegaard (2018). Calibration of material models against TSTM test for crack risk assessment of early-age concrete containing fly ash. *Advances in Materials Science and Engineering*, *2018*, 1069181. https://doi.org/10.1155/2018/1069181

Jirásek, M., & Havlásek, P. (2014). Accurate approximations of concrete creep compliance functions based on continuous retardation spectra. *Computers & Structures*, *135*, 155–168. https://doi.org/10.1016/J.COMPSTRUC.2014.01.024

Klausen, A. E. (2016). E*arly age crack assessment of concrete structures, experimental determination of decisive parameters* [Doctoral dissertation, NTNU].

Klausen, A. E., Kanstad, T., & Bjøntegaard, Ø. (2019). Hardening concrete exposed to realistic curing temperature regimes and restraint conditions: Advanced testing and design methodology. *Advances in Materials Science and Engineering*, *2019*, 9071034. https://doi.org/10.1155/2019/9071034

Klausen, A. E., Kanstad, T., & Bjøntegaard, Ø. (2022). The cracking risk of hardening concrete exposed to realistic curing temperature regimes and restraint conditions—Experimental investigations of important parameters. *Construction and Building Materials*, *338*, 127662. https://doi.org/10.1016/J.CONBUILDMAT.2022.127662

Li, Z., Liang, X., Liu, C., Liang, M., van Breugel, K., & Ye, G. (2022). Thermal deformation and stress of alkali-activated slag concrete under semi-adiabatic condition: Experiments and simulations. *Cement and Concrete Research*, *159*, 106887. https://doi.org/10.1016/j.cemconres.2022.106887

Li, Z., Lu, T., Chen, Y., Wu, B., & Ye, G. (2021). Prediction of the autogenous shrinkage and microcracking of alkali-activated slag and fly ash concrete. *Cement and Concrete Composites*, *117*, 103913. https://doi.org/10.1016/j.cemconcomp.2020.103913

Liang, M., Chang, Z., He, S., Chen, Y., Gan, Y., Schlangen, E., & Šavija, B. (2022). Predicting early-age stress evolution in restrained concrete by thermo-chemo-mechanical model and active ensemble learning. *Computer-Aided Civil and Infrastructure Engineering*, *37*(14), 1809–1833. https://doi.org/10.1111/mice.12915

Liang, M., Chang, Z., Zhang, Y., Cheng, H., He, S., Schlangen, E., & Šavija, B. (2023). Autogenous deformation induced- stress evolution in high-volume GGBFS concrete: Macro-scale behavior and micro-scale origin. *Construction and Building Materials*, *370*, 130663. https://doi.org/10.1016/j.conbuildmat.2023.130663

Liang, M., Li, Z., He, S., Chang, Z., Gan, Y., Schlangen, E., & Šavija, B. (2022). Stress evolution in restrained GGBFS concrete due to autogenous deformation: Bayesian optimization of aging creep. *Construction and Building Materials*, *324*, 126690. https://doi.org/10.1016/J.CONBUILDMAT.2022.126690

Liu, Y., & Schindler, A. K. (2020). Finite-element modeling of early-age concrete stress development. *Journal of Materials in Civil Engineering*, *32*(1), 04019338. https://doi.org/10.1061/(asce)mt.1943-5533.0002988

Lokhorst, S. J. (2001). Deformational behaviour of concrete influenced by hydration related changes of the microstructure. *Delft University of Technology*.

Lura, P., Jensen, O. M., & Weiss, J. (2009). Cracking in cement paste induced by autogenous shrinkage. *Materials and Structures/Materiaux et Constructions*, *42*(8), 1089–1099. https://doi.org/10.1617/s11527-008-9445-z

Lura, P., van Breugel, K., & Maruyama, I. (2001). Effect of curing temperature and type of cement on early-age shrinkage of high-performance concrete. *Cement and Concrete Research*, *31*(12), 1867–1872. https://doi.org/10.1016/S0008-8846(01)00601-9

Maruyama, I., & Lura, P. (2019). Properties of early-age concrete relevant to cracking in massive concrete. *Cement and Concrete Research*, *123*, 105770. https://doi.org/10.1016/J.CEMCONRES.2019.05.015

Nguyen, D. H., Nguyen, V. T., Lura, P., & Dao, V. T. N. (2019). Temperature-stress testing machine—A state-of-the-art design and its unique applications in concrete research. *Cement and Concrete Composites*, *102*, 28–38. https://doi.org/10.1016/J.CEMCONCOMP.2019.04.019

Ou, G., Lin, Z., & Kishi, T. (2023). The practical application of a self-developed temperature stress testing machine in development of expansive concrete blended with calcium sulfoaluminate additives. *Cement and Concrete Research*, *164*, 107045. https://doi.org/10.1016/j.cemconres.2022.107045

Powell, M. J. D. (1978a). A fast algorithm for nonlinearly constrained optimization calculations. In G. A. Watson (Eds.), *Numerical analysis. Lecture notes in mathematics* (Vol. 630., pp. 144–157). Springer. https://doi.org/10.1007/BFb0067703

Powell, M. J. D. (1978b). The convergence of variable metric methods for nonlinearly constrained optimization calculations. In O. L. Mangasarian, R. R. Meyer, & S. M. Robinson (Eds.), *Nonlinear programming 3* (pp. 27–63). Elsevier. https://doi.org/10.1016/B978-0-12-468660-1.50007-4

Semianiuk, V., Tur, V., Herrador, M. F., & Paredes, G. M. (2017). Early age strains and self-stresses of expansive concrete members under uniaxial restraint conditions. *Construction and Building Materials*, *131*, 39–49. https://doi.org/10.1016/J.CONBUILDMAT.2016.11.008

Shen, D., Jiao, Y., Gao, Y., Zhu, S., & Jiang, G. (2020). Influence of ground granulated blast furnace slag on cracking potential of high performance concrete at early age. *Construction and Building Materials*, *241*, 117839. https://doi.org/10.1016/j.conbuildmat.2019.117839

Spingenschmid, R. (1998). Prevention of thermal cracking in concrete at early ages. *E&FN Spon*.

Springenschmid, R., Breitenbücher, R., & Mangold, M. (1994). Development of the cracking frame and the temperature-stress testing machine. *Proceedings of the International RILEM Symposium*, Munich, Germany (pp. 137–144).

Van Breugel, K. (1980). *Relaxation of young concrete*. http://resolver.tudelft.nl/uuid:da1c2e2e-1cef-4583-9deb-9e1c1f548df9

Waltz, R. A., Morales, J. L., Nocedal, J., & Orban, D. (2006). An interior algorithm for nonlinear optimization that combines line search and trust region steps. *Mathematical Programming*, *107*(3), 391–408. https://doi.org/10.1007/s10107-004-0560-5

Wei, Y., Liang, S., Guo, W., & Hansen, W. (2017). Stress prediction in very early-age concrete subject to restraint under varying temperature histories. *Cement and Concrete Composites*, *83*, 45–56. https://doi.org/10.1016/j.cemconcomp.2017.07.006

Wittmann, F. (1974). *Bestimmung physikalischer Eigenschaften des Zementsteins*. Ernst.

Wyrzykowski, M., Hu, Z., Ghourchian, S., Scrivener, K., & Lura, P. (2017). Corrugated tube protocol for autogenous shrinkage measurements: Review and statistical assessment. *Materials and Structures*, *50*(1), 57. https://doi.org/10.1617/s11527-016-0933-2

Xia, Y., Ni, Y., Zhang, P., Liao, W., & Ko, J. (2011). Stress development of a supertall structure during construction: Field monitoring and numerical analysis. *Computer-Aided Civil and Infrastructure Engineering*, *26*(7), 542–559. https://doi.org/10.1111/j.1467-8667.2010.00714.x

Xin, J., Liu, Y., Zhang, G., Wang, Z., Wang, J., Yang, N., & Qiao, Y. (2022). Evaluation of early-age thermal cracking resistance of high w/b, high volume fly ash (HVFA) concrete using temperature stress testing machine. *Case Studies in Construction Materials*, *16*, e00825. https://doi.org/10.1016/j.cscm.2021.e00825

Xin, J., Liu, Y., Zhang, G., Wang, Z., Yang, N., Qiao, Y., & Wang, J. (2021). Comparison of thermal cracking potential evaluation criteria for mass concrete structures. *Materials and Structures*, *54*(6), 243. https://doi.org/10.1617/s11527-021-01840-5

Xin, J., Zhang, G., Liu, Y., Wang, Z., & Wu, Z. (2020). Evaluation of behavior and cracking potential of early-age cementitious systems using uniaxial restraint tests: A review. *Construction and Building Materials*, 231, 117146. https://doi.org/10.1016/j.conbuildmat.2019.117146

Yu, Q., Bažant, P., & Wendner, R. (2012). Improved algorithm for efficient and realistic creep analysis of large creep-sensitive concrete structures. *ACI Structural Journal*, *109*(5), 656–676. https://doi.org/10.14359/51684044

Zhu, H., Hu, Y., Li, Q., & Ma, R. (2020). Restrained cracking failure behavior of concrete due to temperature and shrinkage. *Construction and Building Materials*, *244*, 118318. https://doi.org/10.1016/j.conbuildmat.2020.118318

Zhu, H., Hu, Y., Ma, R., Wang, J., & Li, Q. (2021). Concrete thermal failure criteria, test method, and mechanism: A review. *Construction and Building Materials*, *283*, 122762. https://doi.org/10.1016/j.conbuildmat.2021.122762

How to cite this article: Liang, M., Luzio, G. D., Schlangen, E., & Šavija, B. (2024). Experimentally informed modeling of the early-age stress evolution in cementitious materials using exponential conversion from creep to relaxation. *Computer-Aided Civil and Infrastructure Engineering*, 1–24. https://doi.org/10.1111/mice.13156